

Subaperture-based Digital Aberration Correction for OCT: A Novel Mathematical Approach

Simon Hubmer^{*}, Ekaterina Sherina[†], Ronny Ramlau^{‡§},
Michael Pircher[¶], Rainer Leitgeb^{||}

February 1, 2023

Abstract

In this paper, we consider subaperture-based approaches for the digital aberration correction (DAC) of optical coherence tomography (OCT) images. In particular, we introduce a mathematical framework for describing this class of approaches, resulting in a new understanding of subaperture-correlation method introduced previously. Furthermore, we propose a novel DAC approach requiring only minimal statistical assumptions on the spectral phase of the scanned object. Finally, we demonstrate the applicability of our novel DAC approach via numerical examples based on both simulated and experimental OCT data.

Keywords. Digital Aberration Correction, Subaperture-Correlation, Ophthalmology, Mathematical Modelling, Medical Imaging

1 Introduction

Optical Coherence Tomography (OCT) has found numerous applications in medical imaging, most importantly in ophthalmology [6, 21]. Successful functional extensions of OCT are, e.g., OCT angiography [3, 20], phase sensitive OCT [5, 24], or OCT elastography [15, 32, 35]. OCT provides three-dimensional tissue imaging non-invasively with

^{*}Johann Radon Institute Linz, Altenbergerstraße 69, 4040 Linz, Austria, (simon.hubmer@ricam.oeaw.ac.at), Corresponding author.

[†]University of Vienna, Faculty of Mathematics, Oskar Morgenstern-Platz 1, 1090 Vienna, Austria (ekaterina.sherina@univie.ac.at)

[‡]Johannes Kepler University Linz, Institute of Industrial Mathematics, Altenbergerstraße 69, 4040 Linz, Austria, (ronny.ramlau@jku.at)

[§]Johann Radon Institute Linz, Altenbergerstraße 69, 4040 Linz, Austria, (ronny.ramlau@ricam.oeaw.ac.at)

[¶]Medical University of Vienna, Center for Medical Physics and Biomedical Engineering, Währinger Gürtel 18-20, 1090 Vienna, Austria, (michael.pircher@meduniwien.ac.at)

^{||}Medical University of Vienna, Center for Medical Physics and Biomedical Engineering, Währinger Gürtel 18-20, 1090 Vienna, Austria, (rainer.leitgeb@meduniwien.ac.at)

high axial resolution and excellent structural contrast. The lateral resolution of OCT is decoupled from the axial one, which is determined purely by the partial coherence properties of the light source, whereas the lateral resolution is determined by the numerical aperture of the imaging optics. High spatial resolution is of prime interest for early diagnosis of ocular diseases, when treatment is still most effective and often irreversible functional impairment can be avoided. E.g., first successful gene therapies have been introduced for retinal diseases, as well as cell replacement therapies. All of them call for three-dimensional cellular resolution imaging capability. In case of retinal imaging, cellular resolution has been demonstrated with adaptive optics (AO) assistance, overcoming the substantial aberrations induced by ocular media [10]. AO requires the measurement of wavefront aberrations using a wavefront sensor. Those reconstructed aberrations are then used to pre-shape the wavefront using a deformable mirror leading to diffraction limited imaging performance at the ocular fundus. Combining AO with OCT allows for high isotropic resolution of the retina in all three dimensions [25]. Despite first successful demonstration of AO OCT for retinal diagnostics, additional hardware costs, complex maintenance, and restricted access to AO OCT systems have so far prevented a broader acceptance of the technology. Nevertheless, first clinical prototypes have been introduced recently [34].

Recent demonstrations of high resolution retinal imaging based on OCT signal post-processing alone therefore seemed to be an attractive and cost-effective alternative [13, 23, 33]. Those approaches make use of the complex nature of the OCT signal. The phase information of the OCT signal gives in fact also access to the wavefront aberrations. There have been various methods proposed to extract the wavefront aberrations, being termed digital or computational adaptive optics (DAO, CAO) [1, 16] as well as digital aberration correction (DAC). In the following, we will adapt the notion of DAC. In short, the aim of DAC is to find the wavefront aberrations, and to correct recorded OCT image planes by applying a phase conjugated filter function to their pupil or Fourier plane. Subsequent inverse Fourier transform of the modified pupil plane image leads to an aberration corrected image. This procedure needs to be repeated for each depth plane. Alternatively, if the sample is sufficiently homogeneous, aberration correction only needs to be applied to one plane, the other planes being corrected for known defocus. DAC methods can be roughly distinguished into iterative correction methods and non-iterative methods. Iterative methods assume polynomial expansion [23], e.g., by Zernike polynomials, for the correction phase and determine the set of coefficients leading to optimal image sharpness. Non-iterative methods are inspired by the principle of Shack-Hartman wavefront sensing, by determining local wavefront slopes in the pupil plane and by fitting polynomials to estimate the wavefront aberrations. The first of such methods, termed subaperture DAC [16, 18], splits the pupil plane into a matrix of subdomains and determines the local wavefront slope for each subdomain. A variant of this method uses digital lateral shearing of the pupil phase to retrieve the local wavefront slope for each pixel (DLS DAO) [17]. Both methods have the advantage of being independent of system parameters such as the sample refractive index or of the imaging setup. In principle, DLS DAO provides better sampling and is therefore better suited for higher order aberrations, but it requires specular reflections in the image

plane to be present for proper performance.

In the present paper, we therefore elaborate a mathematical framework for subaperture DAC, which allows both to quantify the limitations of the method as well as leading to strategies to further enhance its performance. In particular, we derive a novel DAC approach which combines the principles of subaperture DAC with a physically motivated averaging.

The outline of this paper is as follows: In Section 2, we recall the general physical background of OCT and its image formation process. In Section 3, we derive a mathematical formalism for general subaperture-based DAC and consider its implications on SC-DAC. In Section 4, we propose a novel DAC approach based on our derived formalism, which in Section 5 we test on both simulated and experimental data, before ending with a short conclusion in Section 6.

2 Physical Background

In this section, we review the physical background on swept source based OCT, as well as on the Shack-Hartmann wavefront sensor.

2.1 Swept Source Based Optical Coherence Tomography

A typical swept source based OCT system for imaging the retina is depicted in Figure 2.1. In short, the light from a tuneable light source (swept source) is coupled into a single mode fiber based interferometer where it is split by the first fiber optic beam splitter (FBS1) into sample and reference arm light, respectively. In the sample arm the light exits the fiber into free space where it is reflected by a scanner (for x - and y -scanning of the sample). The telescope in the sample arm (lenses L2 and L3) is used to image the pivot point of the scanner onto the pupil plane of the eye for scanning the imaging beam across the retina. The light that is backscattered by the retina traverses the optical media where aberrations are introduced, is then de-scanned by the scanner and back-coupled into the single mode fiber by L1. In the reference arm the light traverses an optical delay line to match the path length difference between sample and reference arm and is brought to interference with light returning from the sample arm in the last fiber beam splitter (FBS2).

The interferometric signal is then detected by the balanced detector and digitized by a data acquisition board. To generate a depth profile or an A-scan in OCT the light source is rapidly tuned (swept) over the spectral wavelength band (or wavenumbers k) and the corresponding interferometric signal is recorded simultaneously (cf. Figure 2.2 left). Successive fast Fourier transformation of this interferometric signal results in the final A-scan (cf. Figure 2.2 right). Positive or negative path length differences cannot be distinguished which causes the appearance of a mirror term (cf. grey zone in Figure 2.2 right) that is usually neglected by displaying only the positive path length range. It should be noted that the wavelength sweep is linear in time and in wavenumber $k(= 1/\lambda)$ space (cf. Figure 2.2 left). Assuming a single interface in the sample arm with

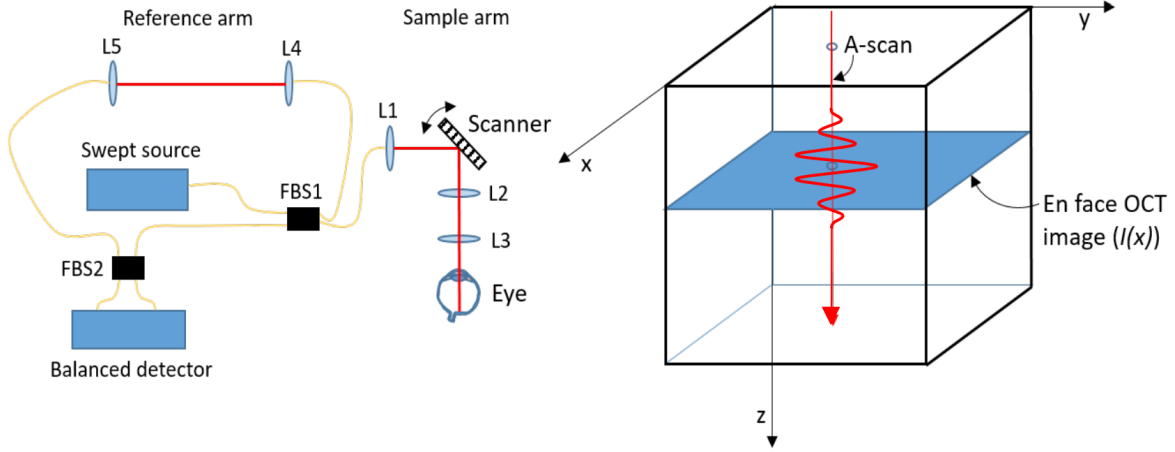


Figure 2.1: Scheme of a typical optical layout of a swept source based OCT system for retinal imaging (left). L1-L5...lenses. FBS1-2... fiber based beam splitter. Coordinate system used in this work (right)

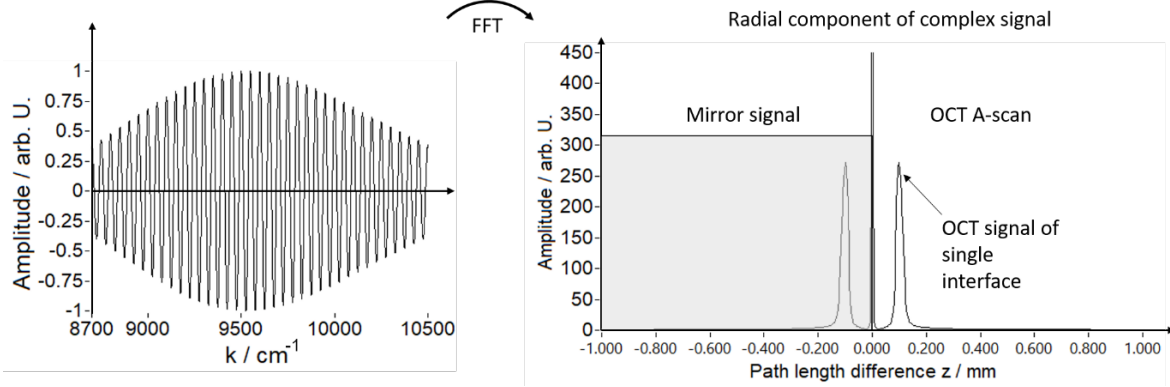


Figure 2.2: Principle of an A-scan generation in OCT of a single interface located at depth position 0.1mm. The wavelength of the tuneable light source is rapidly changed over the entire spectral bandwidth of the source (from 950nm to 1150nm) and the interferometric signal is recorded by the data acquisition board (left). A depth profile or A-scan is retrieved by fast Fourier transformation of the recorded interferogram (in k -space) and by displaying the radial component of the complex valued signal (right). The mirror signal in the grey shaded area (corresponding to negative path length differences) is usually neglected.

reflectivity R_S , the detector current I , depending on the time t or wavenumber k linearly tuned in time t , can be expressed as [4, 22]

$$I(k(t)) = C \left(R_R + R_S(z) + 2\sqrt{R_R R_S(z)} \cos(2k(t)z + \varphi) \right), \quad (2.1)$$

where C is a constant determined by the experimental setup (detector responsivity and illumination power), R_R is the reflectivity in the reference arm, k the wavenumber, z

denotes the optical path length difference between sample and reference arm, and φ is the interferometric phase offset. Fourier transformation of (2.1) with respect to k yields a depth profile or A-scan:

$$A(z) = \int I(k(t)) e^{-2\pi i k(t)z} dk,$$

where $A(z)$ represents a complex valued function. To generate an en-face OCT image (x - y imaging plane) at given depth z , A-scans are recorded at several lateral positions of the sample and the amplitude and phase of $A(z)$ are retrieved at the position z . This complex valued en-face OCT image resulting from the measurement is referred to in the following as $I^m(\mathbf{x})$, the superscript m indicating that the experimentally obtained en-face OCT image may additionally be affected by wavefront aberrations.

2.2 The Shack-Hartmann Wavefront Sensor

In this section, we review some basic properties of the Shack-Hartmann wavefront sensor (SH-WFS) [8, 26, 27], which provides the motivation of the subaperture-based digital aberration correction methods introduced below. First, note that in general the phase or wavefront of light cannot be measured directly, but can be determined from indirect measurements. For example, we saw above that in OCT the phase is encoded in the interference pattern between the sample and the reference field, from which it can be computed; cf. [6, 7]. Among the many different types of wavefront sensors, the SH-WFS described below is perhaps the most commonly used one. A popular alternative is the pyramid wavefront sensor, where the phase is reconstructed from the intensity patterns resulting from light being focused onto the tip of a pyramidal prism [2, 28].

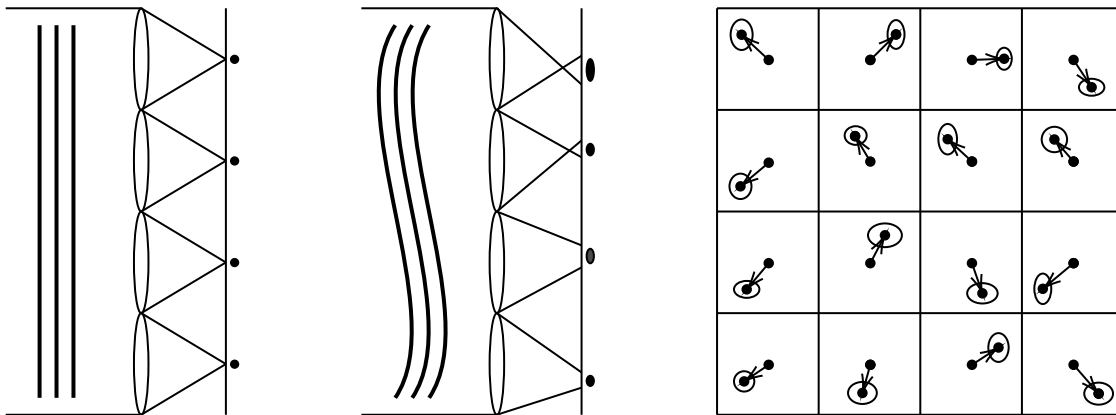


Figure 2.3: Schematic depiction of the physical principle behind the SH-WFS. Light from a distant point source with a plane (non-aberrated) wavefront is focused by lenslets into centered focal spots (Left). If the wavefront is not plane (i.e. aberrated), the focal spots are blurred and shifted with respect to their central locations (Middle). At the CCD detector, these shifts are detected via a comparison of the centers of mass (Right).

The principle of the SH-WFS, schematically depicted in Figure 2.3, can be summarized as follows: The incoming light passes through a quadratic array of small lenses, also called lenslets, which focus the light onto a CCD photon detector, subdivided into a regular grid of so-called subapertures. If the incident light stems from a distant point source with a plane (non-aberrated) wavefront, then each lenslet focuses the light into a focal spot at the center of the corresponding subaperture. However, if the wavefront is not plane (i.e., aberrated), then the focal spots are blurred and shift away from the center of the subapertures. These shifts, typically computed with respect to the centers of mass of the focal spots [9], are measured from the CCD data, and are related to the average gradient (slope) of the incoming wavefront over each subaperture. Hence, from the measured shifts one can reconstruct an approximation of the incoming wavefront, which is itself a non-trivial inverse problem [29] for which many different reconstruction approaches have been proposed. In this paper, we use the fast, stable, and parallelizable Cumulative Reconstructor with Domain Decomposition (CuReD) [30, 31, 36].

3 Subaperture-based Digital Aberration Correction

In this section, we derive a mathematical formalism for subaperture-based DAC approaches. For this, we first recall some basic results on the 2D Fourier transform, and then introduce a mathematical model which connects complex-valued OCT images to wavefront aberrations. Using this model, we then continue by formalizing the subdomains, subapertures, and subimages considered in subaperture-based DAC approaches, which we then use to formalize and review the previously proposed SC-DAC method.

Note that in the following we assume that OCT images are complex-valued functions on \mathbb{R}^2 , which are in practice represented by complex-valued images on a pixel grid.

3.1 Mathematical Preliminaries

The Fourier transform $\mathcal{F}(f)$ of an integrable function $f : \mathbb{R}^2 \rightarrow \mathbb{C}$ is defined by

$$\mathcal{F}(f)(\xi_1, \xi_2) := \int_{-\infty}^{\infty} f(x_1, x_2) e^{-2\pi i (x_1, x_2) \cdot (\xi_1, \xi_2)} d(x_1, x_2).$$

Together with $\mathbf{x} := (x_1, x_2)$ and $\boldsymbol{\xi} := (\xi_1, \xi_2)$ this can be written in the compact form

$$\mathcal{F}(f)(\boldsymbol{\xi}) = \int_{-\infty}^{\infty} f(\mathbf{x}) e^{-2\pi i \mathbf{x} \cdot \boldsymbol{\xi}} d\mathbf{x}.$$

It is well-known that the Fourier transform can be continuously extended to a bounded linear operator $\mathcal{F} : L^2(\mathbb{R}^2) \rightarrow L^2(\mathbb{R}^2)$ and that it is continuously invertible by

$$\mathcal{F}^{-1}(g)(\mathbf{x}) := \int_{-\infty}^{\infty} g(\boldsymbol{\xi}) e^{2\pi i \boldsymbol{\xi} \cdot \mathbf{x}} d\boldsymbol{\xi}.$$

Two useful properties of the Fourier transform are the *translation property*

$$h(\mathbf{x}) := f(\mathbf{x} - \mathbf{x}_0) \implies \mathcal{F}(h)(\boldsymbol{\xi}) = e^{-2\pi i \mathbf{x}_0 \cdot \boldsymbol{\xi}} \mathcal{F}(f)(\boldsymbol{\xi}), \quad (3.1)$$

as well as the *modulation property*

$$h(\mathbf{x}) := e^{2\pi i \mathbf{x} \cdot \boldsymbol{\xi}_0} f(\mathbf{x}) \implies \mathcal{F}(h)(\boldsymbol{\xi}) = \mathcal{F}(f)(\boldsymbol{\xi} - \boldsymbol{\xi}_0), \quad (3.2)$$

which we will make repeated use of in the upcoming analysis. For proofs of these properties as well as further details we refer to the standard literature on Fourier transforms.

3.2 Mathematical Model of Image Formation

In this section, we derive a mathematical model describing the influence of aberrations on the (virtual) image formation process in OCT. The model connects the quantities:

- $I^m = I^m(\mathbf{x})$... the measured complex-valued OCT image, i.e., with aberrations,
- $I = I(\mathbf{x})$... the aberration-free complex-valued OCT image,
- $\phi = \phi(\boldsymbol{\xi})$... the wavefront aberration phase, a real-valued function.

For introducing our mathematical model, it is convenient to make the following

Definition 3.1. Let $I : \mathbb{R}^2 \rightarrow \mathbb{C}$ and $I^m : \mathbb{R}^2 \rightarrow \mathbb{C}$. Then for all $\boldsymbol{\xi} \in \mathbb{R}^2$ we define the Fourier coefficients of I and I^m by

$$D := D(\boldsymbol{\xi}) := \mathcal{F}(I)(\boldsymbol{\xi}), \quad \text{and} \quad D^m := D^m(\boldsymbol{\xi}) := \mathcal{F}(I^m)(\boldsymbol{\xi}).$$

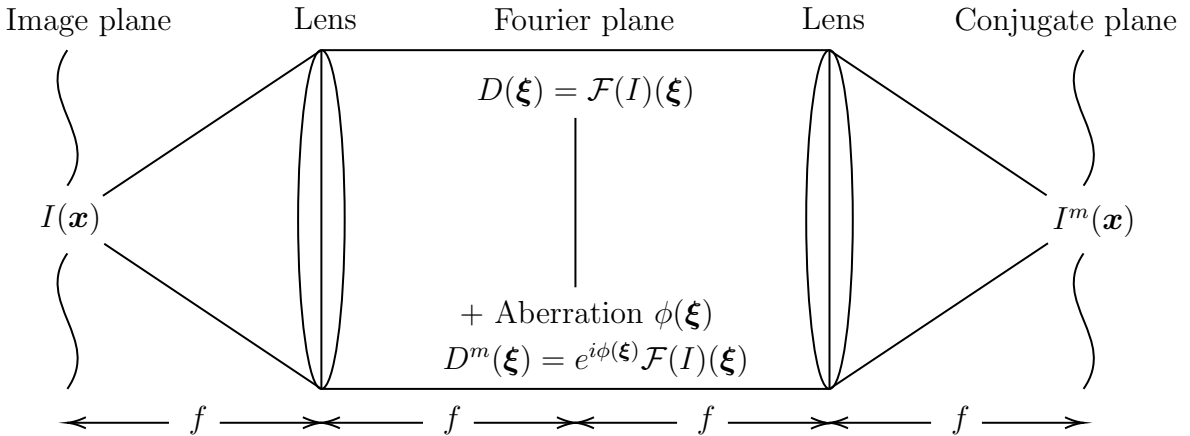


Figure 3.1: Schematic depiction of the virtual image formation model (3.4).

As discussed in Section 2, wavefront aberrations emerge throughout the OCT scanning system. Hence, one way to derive a complete mathematical model of the connection between OCT images and aberrations is to combine the different components in an OCT system into a single mathematical model. However, this is undesirable, since it would require the model to be adapted for every different OCT scanning setup and in

general would also lead to a highly complex model. Hence, in this paper we opt for the following simpler model: It is known [11] that mathematically every imaging system can be simplified to a system containing two properly aligned lenses; cf. Figure 3.1. In this paper, we assume that wavefront aberrations occur predominantly as phase shifts in the Fourier plane; again cf. Figure 3.1. Mathematically, this can be expressed as

$$D^m(\boldsymbol{\xi}) = e^{i\phi(\boldsymbol{\xi})} D(\boldsymbol{\xi}). \quad (3.3)$$

Hence, we obtain the following mathematical model:

Model 1. *The complex-valued functions $I^m \in L^2(\mathbb{R}^2)$ and $I \in L^2(\mathbb{R}^2)$ representing the measured and the aberration-free OCT images, respectively, are assumed to be connected via*

$$I^m(\mathbf{x}) = \mathcal{F}^{-1} \left(e^{i\phi(\boldsymbol{\xi})} \mathcal{F}(I)(\boldsymbol{\xi}) \right) (\mathbf{x}), \quad \forall \mathbf{x} \in \mathbb{R}^2, \quad (3.4)$$

where $\phi \in L^2(\mathbb{R}^2)$ is a real-valued function representing the wavefront-aberrations.

Note that by rearranging the model equation (3.4) we obtain

$$I(\mathbf{x}) = \mathcal{F}^{-1} \left(e^{-i\phi(\boldsymbol{\xi})} \mathcal{F}(I^m)(\boldsymbol{\xi}) \right) (\mathbf{x}), \quad \forall \mathbf{x} \in \mathbb{R}^2. \quad (3.5)$$

Hence, given an estimate of the wavefront aberration ϕ , the aberration-free image I can be reconstructed from the measured image I^m . The aim of DAC is thus to find an estimate of ϕ . However, as can also be seen from (3.4), obtaining this estimate purely from the measured image I^m is impossible without additional assumptions; cf. Section 2.

3.3 Subdomains/Subapertures and Subimages

In this section, we introduce various quantities required for subaperture-based DAC approaches. These can be considered purely from a mathematical point of view, but they also have a motivation stemming from the SH-WFS; see Section 2.2. We start by defining subdomains representing (virtual) subapertures; see also Figure 3.2.

Definition 3.2. For $J, K \in \mathbb{R}^+$ we define the subdomain/subaperture

$$\Omega_{0,0} := [-J/2, J/2) \times [-K/2, K/2) \subset \mathbb{R}^2,$$

as well as the shifted subdomains/subapertures

$$\Omega_{j,k} := T_{j,k}(\Omega_{0,0}) = \{ \boldsymbol{\xi} \in \mathbb{R}^2 \mid T_{j,k}^{-1}(\boldsymbol{\xi}) \in \Omega_{0,0} \}, \quad \forall j, k \in \mathbb{Z},$$

where the translation operator $T_{j,k}$ is defined by

$$T_{j,k}(\boldsymbol{\xi}) := (\xi_1 + jJ, \xi_2 + kK), \quad \forall \boldsymbol{\xi} \in \mathbb{R}^2, \quad \forall j, k \in \mathbb{Z}. \quad (3.6)$$

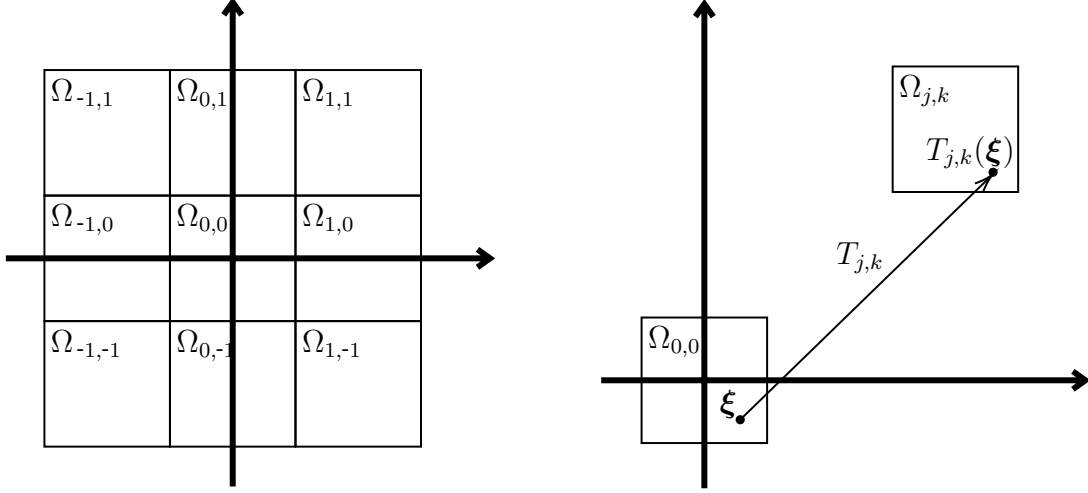


Figure 3.2: Illustration of subdomains $\Omega_{j,k}$ (left) and shift operator $T_{j,k}$ (right).

As the name suggests, we now use the subdomains $\Omega_{j,k}$ as representations of (virtual) subapertures in the Fourier plane for splitting up the OCT image I^m into different (virtual) subimages $I_{j,k}^m$. More precisely, for all $j, k \in \mathbb{Z}$ and $\xi \in \mathbb{R}^2$ let

$$\chi_{j,k}(\xi) := \begin{cases} 1, & \xi \in \Omega_{j,k}, \\ 0, & \text{else,} \end{cases}$$

denote the indicator functions of the subdomains $\Omega_{j,k}$. Then the effect of a subaperture in the Fourier plane on the Fourier coefficients D^m precisely amounts to the “cut-outs”:

$$D_{j,k}^m(\xi) := \chi_{j,k}(\xi) D^m(\xi) \stackrel{(3.3)}{=} \chi_{j,k}(\xi) e^{i\phi(\xi)} \mathcal{F}(I)(\xi), \quad \forall \xi \in \mathbb{R}^2. \quad (3.7)$$

The corresponding (virtual) subimages can now be defined as follows:

Definition 3.3. For each $j, k \in \mathbb{Z}$ the subimages $I_{j,k}^m$ are defined via

$$I_{j,k}^m(\mathbf{x}) := \mathcal{F}^{-1}(D_{j,k}^m(T_{j,k}(\xi)))(\mathbf{x}), \quad \forall \mathbf{x} \in \mathbb{R}^2, \quad (3.8)$$

where the cut-out Fourier data $D_{j,k}^m$ are given by (3.7).

For a better understanding, the definition of the subimages $I_{j,k}^m$ is illustrated in Figure 3.3. Their definition mimicks the image formation process of light being focused through the different lenselets of the SH-WFS. Note that the translation operator $T_{j,k}(\xi)$ appears in (3.7) to model the required shift of the Fourier coefficients to the center of the domain. The above definition implies

Proposition 3.1. Let the subimages $I_{j,k}^m$ be defined as in (3.8) and let

$$\phi_{j,k}(\xi) := \phi(T_{j,k}(\xi)), \quad \forall \xi \in \Omega_{0,0}, \quad \forall j, k \in \mathbb{Z}, \quad (3.9)$$

be the local wavefront aberrations. Then for all $\mathbf{x} \in \mathbb{R}^2$ we obtain the representation

$$I_{j,k}^m(\mathbf{x}) = \mathcal{F}^{-1}(\chi_{0,0}(\xi) e^{i\phi_{j,k}(\xi)} \mathcal{F}(I)(T_{j,k}(\xi)))(\mathbf{x}). \quad (3.10)$$

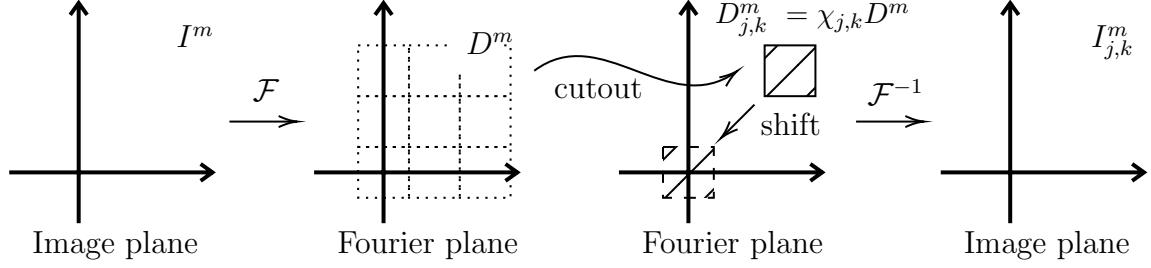


Figure 3.3: Illustration of the definition of the subimages $I_{j,k}^m$ given in (3.8).

Proof. Due to the definitions (3.7) and (3.8) of $D_{j,k}^m$ and $I_{j,k}^m$, respectively, we have

$$I_{j,k}^m(\mathbf{x}) = \mathcal{F}^{-1}(\chi_{j,k}(T_{j,k}(\boldsymbol{\xi}))e^{i\phi(T_{j,k}(\boldsymbol{\xi}))}\mathcal{F}(I)(T_{j,k}(\boldsymbol{\xi}))) (\mathbf{x}).$$

Now, since by the definition of $\chi_{j,k}$ we have

$$\chi_{j,k}(T_{j,k}(\boldsymbol{\xi})) = \chi_{0,0}(\boldsymbol{\xi}),$$

it follows that

$$I_{j,k}^m(\mathbf{x}) = \mathcal{F}^{-1}(\chi_{0,0}(\boldsymbol{\xi})e^{i\phi(T_{j,k}(\boldsymbol{\xi}))}\mathcal{F}(I)(T_{j,k}(\boldsymbol{\xi}))) (\mathbf{x}), \quad (3.11)$$

which together with the definition (3.9) of $\phi_{j,k}$ yields the assertion. \square

Note that if there are no aberrations, i.e., if $\phi(\boldsymbol{\xi}) \equiv 0$, then (3.10) implies

$$I_{j,k}^m(\mathbf{x}) = \mathcal{F}^{-1}(\chi_{0,0}(\boldsymbol{\xi})\mathcal{F}(I)(T_{j,k}(\boldsymbol{\xi}))) (\mathbf{x}).$$

Hence, for the central subimage, i.e., for $j = k = 0$, we obtain

$$I_{0,0}^m(\mathbf{x}) = \mathcal{F}^{-1}(\chi_{0,0}(\boldsymbol{\xi})\mathcal{F}(I)(\boldsymbol{\xi})) (\mathbf{x}),$$

which is a low-resolution version of the original image I . For all other $j, k \neq 0$, the presence of the shift operator $T_{j,k}$ influences the resulting subimage $I_{j,k}^m$. However, note that if I is an OCT image of a single point-source, i.e., $I(x) = \delta(x)$ with δ denoting the delta-distribution, then $\mathcal{F}(I) \equiv 1$. Hence, in this case the shift operator $T_{j,k}$ is not relevant, and thus all subimages $I_{j,k}^m$ are low-resolution versions of the image I . Furthermore, as we shall see below, in case of aberrations, i.e., if $\phi(\boldsymbol{\xi}) \neq 0$, these subimages are shifted depending mainly on the average slope of the wavefront aberration ϕ on the subaperture, i.e., of $\phi_{j,k}$. This fact is leveraged by the subaperture-correlation method.

3.4 The Subaperture-Correlation Method

In this section, we revisit the subaperture-correlation method of [16, 19]. The physical assumptions underlying this method translate to the following mathematical

Assumption 3.1. *On each subaperture $\Omega_{j,k}$, the wavefront aberration ϕ can be reasonably well approximated by a linear function, i.e., for all $j, k \in \mathbb{Z}$ there holds*

$$\phi_{j,k}(\boldsymbol{\xi}) \approx 2\pi (c_{j,k} + \mathbf{s}_{j,k} \cdot \boldsymbol{\xi}) , \quad \forall \boldsymbol{\xi} \in \Omega_{0,0} . \quad (3.12)$$

Furthermore, the Fourier information is self-similar, i.e., for all $j, k \in \mathbb{Z}$ there holds

$$\mathcal{F}(I)(T_{j,k}(\boldsymbol{\xi})) \approx \mathcal{F}(I)(\boldsymbol{\xi}) , \quad \forall \boldsymbol{\xi} \in \Omega_{0,0} . \quad (3.13)$$

Using these assumptions, we are able to derive the following

Proposition 3.2. *Let $I_{j,k}^m$ be defined as in (3.8) and let Assumption 3.1 hold. Then*

$$|I_{j,k}^m(\mathbf{x} - (\mathbf{s}_{j,k} - \mathbf{s}_{0,0}))| \approx |I_{0,0}^m(\mathbf{x})| , \quad \forall j, k \in \mathbb{Z} . \quad (3.14)$$

Proof. First, note that by using (3.12) in (3.10) it follows that

$$\begin{aligned} I_{j,k}^m(\mathbf{x}) &= \mathcal{F}^{-1} \left(\chi_{0,0}(\boldsymbol{\xi}) e^{i\phi_{j,k}(\boldsymbol{\xi})} \mathcal{F}(I)(T_{j,k}(\boldsymbol{\xi})) \right) (\mathbf{x}) \\ &\approx \mathcal{F}^{-1} \left(\chi_{0,0}(\boldsymbol{\xi}) e^{2\pi i(c_{j,k} + \mathbf{s}_{j,k} \cdot \boldsymbol{\xi})} \mathcal{F}(I)(T_{j,k}(\boldsymbol{\xi})) \right) (\mathbf{x}) , \end{aligned}$$

which together with (3.2) implies that

$$\begin{aligned} I_{j,k}^m(\mathbf{x}) &\approx \mathcal{F}^{-1} \left(\chi_{0,0}(\boldsymbol{\xi}) e^{2\pi i(c_{j,k} + \mathbf{s}_{j,k} \cdot \boldsymbol{\xi})} \mathcal{F}(I)(T_{j,k}(\boldsymbol{\xi})) \right) (\mathbf{x}) , \\ &= e^{2\pi i c_{j,k}} \mathcal{F}^{-1} \left(\chi_{0,0}(\boldsymbol{\xi}) \mathcal{F}(I)(T_{j,k}(\boldsymbol{\xi})) \right) (\mathbf{x} + \mathbf{s}_{j,k}) . \end{aligned}$$

Together with (3.13) it follows that

$$I_{j,k}^m(\mathbf{x}) \approx e^{2\pi i c_{j,k}} \mathcal{F}^{-1} \left(\chi_{0,0}(\boldsymbol{\xi}) \mathcal{F}(I) \right) (\mathbf{x} + \mathbf{s}_{j,k}) ,$$

which can be rewritten into

$$e^{-2\pi i c_{j,k}} I_{j,k}^m(\mathbf{x} - \mathbf{s}_{j,k}) \approx \mathcal{F}^{-1} \left(\chi_{0,0}(\boldsymbol{\xi}) \mathcal{F}(I) \right) (\mathbf{x}) .$$

Since this holds in particular for $j = k = 0$, we obtain

$$e^{-2\pi i c_{j,k}} I_{j,k}^m(\mathbf{x} - \mathbf{s}_{j,k}) \approx e^{-2\pi i c_{0,0}} I_{0,0}^m(\mathbf{x} - \mathbf{s}_{0,0}) , \quad \forall j, k \in \mathbb{Z} .$$

Hence, taking the absolute value on both sides we obtain

$$|I_{j,k}^m(\mathbf{x} - \mathbf{s}_{j,k})| \approx |I_{0,0}^m(\mathbf{x} - \mathbf{s}_{0,0})| , \quad \forall j, k \in \mathbb{Z} ,$$

which after the change of variables $\mathbf{x} \rightarrow \mathbf{x} + \mathbf{s}_{0,0}$ yields the assertion. \square

In [16, 19] the connection (3.14) is used to estimate the relative shifts $(\mathbf{s}_{j,k} - \mathbf{s}_{0,0})$ by matching the subimages $I_{j,k}^m$ and $I_{0,0}^m$. From these shifts the full wavefront aberration function ϕ is reconstructed via a least squares fitting onto either a piecewise linear or a Zernike polynomial basis. The subaperture-corellation method can thus be summarized into the following:

Algorithm 1 (Subaperture-Correlation Method).

1. For given I^m and each $j, k \in \mathbb{Z}$ compute the subimages $I_{j,k}^m$ defined in (3.8).
2. Estimate the relative slopes $(\mathbf{s}_{j,k} - \mathbf{s}_{0,0})$ through image fitting using (3.14).
3. Reconstruct the wavefront aberration ϕ from the relative slopes $(\mathbf{s}_{j,k} - \mathbf{s}_{0,0})$.
4. Compute the corrected image by applying the phase correction (3.5).

Concerning the second step in the above algorithm, note that instead of via image fitting, the relative slopes $(\mathbf{s}_{j,k} - \mathbf{s}_{0,0})$ can also be computed explicitly, as we see in

Proposition 3.3. *Let $I_{j,k}^m$ be defined as in (3.8) and let Assumption 3.1 hold. Then*

$$\mathbf{s}_{j,k} - \mathbf{s}_{0,0} \approx \frac{\int_{\mathbb{R}^2} \mathbf{x} |I_{0,0}^m(\mathbf{x})| d\mathbf{x}}{\int_{\mathbb{R}^2} |I_{0,0}^m(\mathbf{x})| d\mathbf{x}} - \frac{\int_{\mathbb{R}^2} \mathbf{x} |I_{j,k}^m(\mathbf{x})| d\mathbf{x}}{\int_{\mathbb{R}^2} |I_{j,k}^m(\mathbf{x})| d\mathbf{x}}, \quad \forall j, k \in \mathbb{Z}. \quad (3.15)$$

Proof. Let $j, k \in \mathbb{Z}$ be arbitrary but fixed. Due to (3.14) there holds

$$|I_{j,k}^m(\mathbf{x} - (\mathbf{s}_{j,k} - \mathbf{s}_{0,0}))| \approx |I_{0,0}^m(\mathbf{x})|.$$

Computing the center of mass on both sides we obtain

$$\frac{\int_{\mathbb{R}^2} \mathbf{x} |I_{j,k}^m(\mathbf{x} - (\mathbf{s}_{j,k} - \mathbf{s}_{0,0}))| d\mathbf{x}}{\int_{\mathbb{R}^2} |I_{j,k}^m(\mathbf{x} - (\mathbf{s}_{j,k} - \mathbf{s}_{0,0}))| d\mathbf{x}} \approx \frac{\int_{\mathbb{R}^2} \mathbf{x} |I_{0,0}^m(\mathbf{x})| d\mathbf{x}}{\int_{\mathbb{R}^2} |I_{0,0}^m(\mathbf{x})| d\mathbf{x}}. \quad (3.16)$$

Next, note that by a simple change of variables in the integral we obtain

$$\int_{\mathbb{R}^2} \mathbf{x} |I_{j,k}^m(\mathbf{x} - (\mathbf{s}_{j,k} - \mathbf{s}_{0,0}))| d\mathbf{x} = \int_{\mathbb{R}^2} \mathbf{x} |I_{j,k}^m(\mathbf{x})| d\mathbf{x} + (\mathbf{s}_{j,k} - \mathbf{s}_{0,0}) \int_{\mathbb{R}^2} |I_{j,k}^m(\mathbf{x})| d\mathbf{x}.$$

Together with the fact that

$$\int_{\mathbb{R}^2} |I_{j,k}^m(\mathbf{x} - (\mathbf{s}_{j,k} - \mathbf{s}_{0,0}))| d\mathbf{x} = \int_{\mathbb{R}^2} |I_{j,k}^m(\mathbf{x})| d\mathbf{x},$$

we obtain that (3.16) is equivalent to

$$\frac{\int_{\mathbb{R}^2} \mathbf{x} |I_{j,k}^m(\mathbf{x})| d\mathbf{x} + (\mathbf{s}_{j,k} - \mathbf{s}_{0,0}) \int_{\mathbb{R}^2} |I_{j,k}^m(\mathbf{x})| d\mathbf{x}}{\int_{\mathbb{R}^2} |I_{j,k}^m(\mathbf{x})| d\mathbf{x}} \approx \frac{\int_{\mathbb{R}^2} \mathbf{x} |I_{0,0}^m(\mathbf{x})| d\mathbf{x}}{\int_{\mathbb{R}^2} |I_{0,0}^m(\mathbf{x})| d\mathbf{x}}.$$

which after a reordering of the terms now yields the assertion. \square

Note that for the third step in Algorithm 1, any wavefront reconstruction method for the SH-WFS such as the CuReD method introduced in Section 2.2 can be used. Note that condition (3.13) is satisfied if I is the OCT image of a distant point source, since then $\mathcal{F}(I) \equiv 1$. Furthermore, it was found experimentally in [16, 19] that condition (3.13) is essential for the subaperture-correlation method to work satisfactorily.

However, while in many cases the Fourier information is self-similar and thus (3.13) is satisfied, this ultimately depends on the structure of the considered objects, thus limiting its applicability. Hence, it is desirable to find a DAC approach which does not require a condition like (3.13). However, we already indicated that a DAC approach requires some type of assumption. Thus, in the next section we will only use a minimal additional assumption, which has a statistical justification and leads to a novel subaperture-based DAC approach.

4 A Novel Correction Approach

In this section, we present a novel aberration correction approach for OCT based on virtual subapertures, a statistical distribution assumption, and a suitable averaging.

4.1 Motivation and Key Ideas

The following approach is motivated by the observation that in hardware-based AO-OCT as used, e.g., in ophthalmology, the wavefront sensing is typically complemented with an averaging process to remove the speckle noise due to the object structure [14]. The averaging blurs out the object structure phase of the OCT image and leaves only the wavefront error to be detected, resulting in more well-defined focal spots on the SH-WFS and more accurate wavefront aberration measurements. Mathematically, this indicates that the spectral phase and the wavefront phase are generally of a different frequency, and can thus be distinguished from each other.

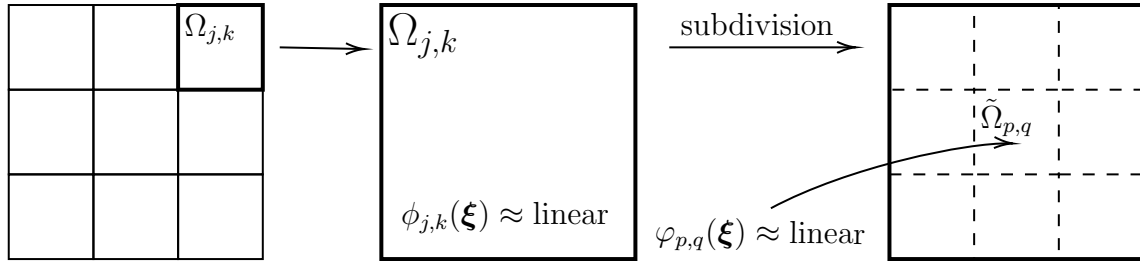


Figure 4.1: Illustration of the mathematical setting used in our novel DAC method: Subdivision of \mathbb{R}^2 into subdomains $\Omega_{j,k}$ (left), single subdomain $\Omega_{j,k}$ and assumption that $\phi_{j,k}$ is approximately linear on $\Omega_{j,k}$ (middle), subdivision of $\Omega_{j,k}$ into smaller subdomains $\tilde{\Omega}_{p,q}$ and assumption that $\varphi_{p,q}$ is approximately linear on $\Omega_{p,q}$ (right).

In order to use these observations for deriving a novel DAC approach, we now consider the Fourier transform $\mathcal{F}(I)$ and note that it can be written in the polar form

$$\mathcal{F}(I)(\boldsymbol{\xi}) = |\mathcal{F}(I)(\boldsymbol{\xi})| e^{i\varphi(\boldsymbol{\xi})}, \quad (4.1)$$

where $|\mathcal{F}(I)(\boldsymbol{\xi})|$ is called the *spectral amplitude* of I , and the real valued function $\varphi(\boldsymbol{\xi})$ denotes the angular component of $\mathcal{F}(I)$, and is referred to as the *spectral phase*.

In order to translate the physical observations made above into a mathematically useful form, we return again to the subapertures $\Omega_{j,k}$. As before, we will assume that the wavefront aberration ϕ can be reasonably well approximated by linear functions $\phi_{j,k}$ on the subdomains $\Omega_{j,k}$. Next, we translate the physical observation that the spectral phase φ introduced by the object contains higher frequencies than the phase ϕ corresponding to the wavefront aberrations. For this, we subdivide each subaperture $\Omega_{j,k}$ into a number of smaller subapertures $\tilde{\Omega}_{p,q}$. While the precise definition is given below, for now we refer to the illustration given in Figure 4.1. On each of the smaller subdomains $\tilde{\Omega}_{p,q}$ we now approximate the spectral phase φ by a linear function $\varphi_{p,q}$. Then, the physical observation that the highly oscillatory spectral phase φ causes generally random phase shifts translates to the mathematical statement that the slopes of $\varphi_{p,q}$ are randomly distributed with a zero mean. We now proceed to make these statements mathematically precise.

4.2 Subdomains/Subapertures and Subimages Revisited

In order to mathematically specify the physical assumptions made above, we need to adapt the definitions of subdomains/subapertures and the resulting subimages made in Section 3.3. We start with the definition of the subdivisions of the subdomains $\Omega_{j,k}$.

Definition 4.1. For $P, Q \in \mathbb{R}^+$ we define the subdomain/subaperture

$$\tilde{\Omega}_{0,0} := [-P/2, P/2) \times [-Q/2, Q/2) \subset \mathbb{R}^2,$$

as well as the shifted subdomains/subapertures

$$\tilde{\Omega}_{p,q} := \tilde{T}_{p,q}(\tilde{\Omega}_{0,0}) = \left\{ \boldsymbol{\xi} \in \mathbb{R}^2 \mid \tilde{T}_{p,q}^{-1}(\boldsymbol{\xi}) \in \tilde{\Omega}_{0,0} \right\}, \quad \forall p, q \in \mathbb{Z},$$

where the translation operator $\tilde{T}_{p,q}$ is defined by

$$\tilde{T}_{p,q}(\boldsymbol{\xi}) := (\xi_1 + pP, \xi_2 + qQ), \quad \forall \boldsymbol{\xi} \in \mathbb{R}^2, \quad \forall p, q \in \mathbb{Z}. \quad (4.2)$$

Throughout this manuscript, we assume that J, K are multiples of P, Q , i.e.,

$$\exists l_1, l_2 \in \mathbb{N} : \quad J = l_1 P, \quad \text{and} \quad K = l_2 Q. \quad (4.3)$$

This implies that every subdomain $\Omega_{j,k}$ can be uniquely decomposed into a finite union of the subdomains $\tilde{\Omega}_{p,q}$; see Figure 4.1. More precisely, if we define the index sets

$$\Delta_{j,k} := \left\{ (p, q) \in \mathbb{Z}^2 \mid \tilde{\Omega}_{p,q} \subseteq \Omega_{j,k} \right\},$$

then (4.3) implies that

$$\Omega_{j,k} = \bigcup_{p,q \in \Delta_{j,k}} \tilde{\Omega}_{p,q}.$$

Now as before, for all $p, q \in \mathbb{Z}$ and $\boldsymbol{\xi} \in \mathbb{R}^2$ we consider the indicator functions

$$\tilde{\chi}_{p,q}(\boldsymbol{\xi}) := \begin{cases} 1, & \boldsymbol{\xi} \in \tilde{\Omega}_{p,q}, \\ 0, & \text{else.} \end{cases}$$

of the subdomains $\tilde{\Omega}_{p,q}$, and define the following “cut-outs” of the Fourier coefficients:

$$\tilde{D}_{p,q}^m(\boldsymbol{\xi}) := \tilde{\chi}_{p,q}(\boldsymbol{\xi}) D^m(\boldsymbol{\xi}) = \tilde{\chi}_{p,q}(\boldsymbol{\xi}) e^{i\phi(\boldsymbol{\xi})} \mathcal{F}(I)(\boldsymbol{\xi}), \quad \forall \boldsymbol{\xi} \in \mathbb{R}^2. \quad (4.4)$$

The subimages corresponding to those Fourier “cut-outs” are given in the following

Definition 4.2. For each $p, q \in \mathbb{Z}$, the subimages $\tilde{I}_{p,q}^m$ are defined via

$$\tilde{I}_{p,q}^m(\mathbf{x}) := \mathcal{F}^{-1}(\tilde{D}_{p,q}^m(\tilde{T}_{p,q}(\boldsymbol{\xi}))) (\mathbf{x}), \quad \forall \mathbf{x} \in \mathbb{R}^2, \quad (4.5)$$

where the cut-out Fourier data $\tilde{D}_{p,q}^m$ are given by (4.4).

Similarly to Proposition 3.1, we can derive an alternative representation in

Proposition 4.1. Let the subimages $\tilde{I}_{p,q}^m$ be as defined in (4.5) and let

$$\tilde{\phi}_{p,q}(\boldsymbol{\xi}) := \phi(\tilde{T}_{p,q}(\boldsymbol{\xi})), \quad \forall \boldsymbol{\xi} \in \tilde{\Omega}_{0,0}, \quad \forall p, q \in \mathbb{Z}, \quad (4.6)$$

denote the local wavefront aberrations. Then we obtain the representation

$$\tilde{I}_{p,q}^m(\mathbf{x}) = \mathcal{F}^{-1} \left(\tilde{\chi}_{0,0}(\boldsymbol{\xi}) e^{i\tilde{\phi}_{p,q}(\boldsymbol{\xi})} \mathcal{F}(I)(\tilde{T}_{p,q}(\boldsymbol{\xi})) \right) (\mathbf{x}). \quad (4.7)$$

Proof. This follows in direct analogy to the proof of Proposition 3.1. \square

4.3 Mathematical Derivation of the Method

The physical motivation and key ideas introduced in Section 4.1 now translate to

Assumption 4.1. On each subaperture $\Omega_{j,k}$, the wavefront aberration ϕ can be reasonably well approximated by a linear function, i.e., (3.12) holds for all $j, k \in \mathbb{Z}$, i.e.,

$$\phi_{j,k}(\boldsymbol{\xi}) \approx 2\pi (c_{j,k} + \mathbf{s}_{j,k} \cdot \boldsymbol{\xi}), \quad \forall \boldsymbol{\xi} \in \Omega_{0,0}.$$

Furthermore, on each smaller subaperture $\tilde{\Omega}_{p,q}$, the spectral phase φ can also be reasonably well approximated by a linear function, i.e., for all $p, q \in \mathbb{Z}$ there holds

$$\varphi_{p,q}(\boldsymbol{\xi}) := \varphi(\tilde{T}_{p,q}(\boldsymbol{\xi})) \approx 2\pi (d_{p,q} + \mathbf{t}_{p,q} \cdot \boldsymbol{\xi}), \quad \forall \boldsymbol{\xi} \in \tilde{\Omega}_{0,0}. \quad (4.8)$$

Moreover, the magnitude of the Fourier information is self-similar, i.e., for all $p, q \in \mathbb{Z}$,

$$\left| \mathcal{F}(I)(\tilde{T}_{p,q}(\boldsymbol{\xi})) \right| \approx |\mathcal{F}(I)(\boldsymbol{\xi})|, \quad \forall \boldsymbol{\xi} \in \tilde{\Omega}_{0,0}. \quad (4.9)$$

Finally, let $J, K, P, Q \in \mathbb{R}^+$ satisfy the multiplicity condition (4.3), and let

$$\sum_{p,q \in \Delta_{j,k}} (\mathbf{t}_{p,q} - \mathbf{t}_{0,0}) \approx 0, \quad \forall j, k \in \mathbb{Z}. \quad (4.10)$$

Note first that (4.10) encodes the physical observation that averaging blurs out the spectral phase of the OCT image: as we will see below, the relative slopes $(\mathbf{t}_{p,q} - \mathbf{t}_{0,0})$ cause local shifts in the subimages $\tilde{I}_{p,q}^m$ on a smaller scale than those induced by the relative slopes $(\mathbf{s}_{j,k} - \mathbf{s}_{0,0})$. The fact that in hardware-based AO with a SH-WFS these local shifts can be removed by averaging thus motivates (4.10). Furthermore, note that in contrast to (3.13), we now only require that the spectral amplitude $|\mathcal{F}(I)|$ is self-similar. Since due to (3.4) the wavefront aberration ϕ acts only on the spectral phase φ but not on the spectral amplitude $|\mathcal{F}(I)|$, this assumption can always be satisfied by redefining the OCT image I^m to have a constant spectral amplitude.

For the upcoming derivation, we first need the following technical result:

Proposition 4.2. *Let Assumption 4.1 hold, let $j, k \in \mathbb{Z}$ and let $p, q \in \Delta_{j,k}$. Then with $\tilde{c}_{j,k}(p, q) := c_{j,k} + \mathbf{s}_{j,k} \cdot (pP - jJ, qQ - kK)$ the function $\tilde{\phi}_{p,q}$ defined in (4.6) satisfies*

$$\tilde{\phi}_{p,q}(\boldsymbol{\xi}) \approx 2\pi (\tilde{c}_{j,k}(p, q) + \mathbf{s}_{j,k} \cdot \boldsymbol{\xi}) , \quad \forall \boldsymbol{\xi} \in \tilde{\Omega}_{0,0} ,$$

Proof. Let $j, k \in \mathbb{Z}$, $p, q \in \Delta_{j,k}$, and $\boldsymbol{\xi} \in \tilde{\Omega}_{0,0}$, be arbitrary but fixed and consider

$$\tilde{\phi}_{p,q}(\boldsymbol{\xi}) \stackrel{(4.6)}{=} \phi(\tilde{T}_{p,q}(\boldsymbol{\xi})) \stackrel{(4.2)}{=} \phi(\xi_1 + pP, \xi_2 + qQ) .$$

Since due to (3.6) and (3.9) there holds

$$\begin{aligned} \phi(\xi_1 + pP, \xi_2 + qQ) &= \phi((\xi_1 + pP - jJ) + jJ, (\xi_2 + qQ - kK) + kK) \\ &\stackrel{(3.6)}{=} \phi(T_{j,k}(\xi_1 + pP - jJ, \xi_2 + qQ - kK)) \\ &\stackrel{(3.9)}{=} \phi_{j,k}(\xi_1 + pP - jJ, \xi_2 + qQ - kK) , \end{aligned}$$

it follows that

$$\tilde{\phi}_{p,q}(\boldsymbol{\xi}) = \phi_{j,k}(\xi_1 + pP - jJ, \xi_2 + qQ - kK) .$$

Now since $\boldsymbol{\xi} \in \tilde{\Omega}_{0,0}$ and $p, q \in \Delta_{j,k}$ it follows that $(\xi_1 + pP - jJ, \xi_2 + qQ - kK) \in \Omega_{0,0}$. Hence, it follows with (3.12) that

$$\begin{aligned} \tilde{\phi}_{p,q}(\boldsymbol{\xi}) &= \phi_{j,k}(\xi_1 + pP - jJ, \xi_2 + qQ - kK) \\ &\approx 2\pi (c_{j,k} + \mathbf{s}_{j,k} \cdot (\xi_1 + pP - jJ, \xi_2 + qQ - kK)) \\ &= 2\pi (c_{j,k} + \mathbf{s}_{j,k} \cdot (pP - jJ, qQ - kK) + \mathbf{s}_{j,k} \cdot \boldsymbol{\xi}) , \end{aligned}$$

which together with the definition of $\tilde{c}_{j,k}(p, q)$ now yields the assertion. \square

Using the above proposition, we can now proceed to the following

Theorem 4.3. *Let $\tilde{I}_{p,q}^m$ be defined as in (4.5) and let (3.4) and Assumption 4.1 hold. Then for each $j, k \in \mathbb{Z}$, any $p, q \in \Delta_{j,k}$, and for all $\mathbf{x} \in \mathbb{R}^2$ there holds*

$$\left| \tilde{I}_{p,q}^m(\mathbf{x} - ((\mathbf{s}_{j,k} - \mathbf{s}_{0,0}) + (\mathbf{t}_{p,q} - \mathbf{t}_{0,0}))) \right| \approx \left| \tilde{I}_{0,0}^m(\mathbf{x}) \right| . \quad (4.11)$$

Proof. Let $j, k \in \mathbb{Z}$ be arbitrary but fixed and let $p, q \in \Delta_{j,k}$. Due to (4.7) there holds

$$\tilde{I}_{p,q}^m(\mathbf{x}) = \mathcal{F}^{-1} \left(\tilde{\chi}_{0,0}(\boldsymbol{\xi}) e^{i\tilde{\phi}_{p,q}(\boldsymbol{\xi})} \mathcal{F}(I)(\tilde{T}_{p,q}(\boldsymbol{\xi})) \right) (\mathbf{x}).$$

Since due to Proposition 4.2 there holds

$$\tilde{\phi}_{p,q}(\boldsymbol{\xi}) \approx 2\pi (\tilde{c}_{j,k}(p, q) + \mathbf{s}_{j,k} \cdot \boldsymbol{\xi}), \quad \forall \boldsymbol{\xi} \in \tilde{\Omega}_{0,0},$$

it follows that

$$\tilde{I}_{p,q}^m(\mathbf{x}) \approx \mathcal{F}^{-1} \left(\tilde{\chi}_{0,0}(\boldsymbol{\xi}) e^{2\pi i(\tilde{c}_{j,k}(p, q) + \mathbf{s}_{j,k} \cdot \boldsymbol{\xi})} \mathcal{F}(I)(\tilde{T}_{p,q}(\boldsymbol{\xi})) \right) (\mathbf{x}),$$

which can be rearranged into

$$\tilde{I}_{p,q}^m(\mathbf{x}) \approx e^{2\pi i \tilde{c}_{j,k}(p, q)} \mathcal{F}^{-1} \left(\tilde{\chi}_{0,0}(\boldsymbol{\xi}) e^{2\pi i \mathbf{s}_{j,k} \cdot \boldsymbol{\xi}} \mathcal{F}(I)(\tilde{T}_{p,q}(\boldsymbol{\xi})) \right) (\mathbf{x}). \quad (4.12)$$

Next, note that due to (4.1) and (4.8) for all $\boldsymbol{\xi} \in \tilde{\Omega}_{0,0}$ there holds

$$\mathcal{F}(I)(\tilde{T}_{p,q}(\boldsymbol{\xi})) \stackrel{(4.1)}{=} \left| \mathcal{F}(I)(\tilde{T}_{p,q}(\boldsymbol{\xi})) \right| e^{i\varphi(\tilde{T}_{p,q}(\boldsymbol{\xi}))} \stackrel{(4.8)}{\approx} \left| \mathcal{F}(I)(\tilde{T}_{p,q}(\boldsymbol{\xi})) \right| e^{i2\pi(d_{p,q} + \mathbf{t}_{p,q} \cdot \boldsymbol{\xi})}$$

Using this in (4.12) and after rearranging we obtain

$$\tilde{I}_{p,q}^m(\mathbf{x}) \approx e^{2\pi i(\tilde{c}_{j,k}(p, q) + d_{p,q})} \mathcal{F}^{-1} \left(\tilde{\chi}_{0,0}(\boldsymbol{\xi}) e^{2\pi i(\mathbf{s}_{j,k} + \mathbf{t}_{p,q}) \cdot \boldsymbol{\xi}} \left| \mathcal{F}(I)(\tilde{T}_{p,q}(\boldsymbol{\xi})) \right| \right) (\mathbf{x}),$$

which together with (3.2) and after taking the absolute value yields

$$\left| \tilde{I}_{p,q}^m(\mathbf{x}) \right| \approx \left| \mathcal{F}^{-1} \left(\tilde{\chi}_{0,0}(\boldsymbol{\xi}) \left| \mathcal{F}(I)(\tilde{T}_{p,q}(\boldsymbol{\xi})) \right| \right) (\mathbf{x} + (\mathbf{s}_{j,k} + \mathbf{t}_{p,q})) \right|. \quad (4.13)$$

Next, note that due to the self-similarity assumption (3.13) it follows that

$$\left| \tilde{I}_{p,q}^m(\mathbf{x}) \right| \approx \left| \mathcal{F}^{-1} (\tilde{\chi}_{0,0}(\boldsymbol{\xi}) |\mathcal{F}(I)(\boldsymbol{\xi})|) (\mathbf{x} + (\mathbf{s}_{j,k} + \mathbf{t}_{p,q})) \right|,$$

and thus after the change of variables $\mathbf{x} \rightarrow \mathbf{x} - (\mathbf{s}_{j,k} + \mathbf{t}_{p,q})$ we obtain

$$\left| \tilde{I}_{p,q}^m(\mathbf{x} - (\mathbf{s}_{j,k} + \mathbf{t}_{p,q})) \right| \approx \left| \mathcal{F}^{-1} (\tilde{\chi}_{0,0}(\boldsymbol{\xi}) |\mathcal{F}(I)(\boldsymbol{\xi})|) (\mathbf{x}) \right|.$$

Since the indices $j, k \in \mathbb{Z}$ and $p, q \in \Delta_{j,k}$ were arbitrary but fixed, and since the right hand side in the above equation is independent of j, k, p, q , it follows that

$$\left| \tilde{I}_{p,q}^m(\mathbf{x} - (\mathbf{s}_{j,k} + \mathbf{t}_{p,q})) \right| \approx \left| \tilde{I}_{0,0}^m(\mathbf{x} - (\mathbf{s}_{0,0} + \mathbf{t}_{0,0})) \right|,$$

which after the change of variables $\mathbf{x} \rightarrow \mathbf{x} + (\mathbf{s}_{0,0} + \mathbf{t}_{0,0})$ yields the assertion. \square

As in the subaperture-correlation method, due to (4.11) the relative shift vectors $\mathbf{v}_{j,k,p,q} := (\mathbf{s}_{j,k} - \mathbf{s}_{0,0}) + (\mathbf{t}_{p,q} - \mathbf{t}_{0,0})$ can now be estimated by matching the subimages $\tilde{I}_{p,q}^m$ and $\tilde{I}_{0,0}^m$. Summing these vectors $\mathbf{v}_{j,k,p,q}$ over all $p, q \in \Delta_{j,k}$ for fixed $j, k \in \mathbb{Z}$ yields

$$\sum_{p,q \in \Delta_{j,k}} \mathbf{v}_{j,k,p,q} = \sum_{p,q \in \Delta_{j,k}} (\mathbf{s}_{j,k} - \mathbf{s}_{0,0}) + \sum_{p,q \in \Delta_{j,k}} (\mathbf{t}_{p,q} - \mathbf{t}_{0,0}) .$$

Noting that $\mathbf{s}_{j,k}$ is independent of $p, q \in \Delta_{j,k}$ and using (4.10) we thus obtain

$$\mathbf{s}_{j,k} - \mathbf{s}_{0,0} \approx \frac{1}{|\Delta_{j,k}|} \sum_{p,q \in \Delta_{j,k}} \mathbf{v}_{j,k,p,q} , \quad (4.14)$$

where $|\Delta_{j,k}|$ denotes the number of elements in the set $\Delta_{j,k}$. These considerations now give rise to our novel DAC approach, which is summarized in the following

Algorithm 2 (Novel Digital Aberration Correction Method).

1. For given I^m and each $p, q \in \mathbb{Z}$ compute the subimages $\tilde{I}_{p,q}^m$ defined in (4.5).
2. Estimate the shift vectors $\mathbf{v}_{j,k,p,q} = (\mathbf{s}_{j,k} - \mathbf{s}_{0,0}) + (\mathbf{t}_{p,q} - \mathbf{t}_{0,0})$ through image fitting using (4.11).
3. Compute the relative slopes $\mathbf{s}_{j,k} - \mathbf{s}_{0,0}$ via averaging as in formula (4.14).
4. Reconstruct the wavefront aberration ϕ from the relative slopes $(\mathbf{s}_{j,k} - \mathbf{s}_{0,0})$.
5. Compute the corrected image by applying the phase correction (3.5).

Concerning the second and third step in the above algorithm, note that similarly as in Proposition 3.1, the relative slopes $(\mathbf{s}_{j,k} - \mathbf{s}_{0,0})$ can also be computed explicitly, as we now show in

Proposition 4.4. *Let $\tilde{I}_{p,q}^m$ be defined as in (4.5) and let Assumption 4.1 hold. Then*

$$\mathbf{s}_{j,k} - \mathbf{s}_{0,0} \approx \frac{1}{|\Delta_{j,k}|} \sum_{p,q \in \Delta_{j,k}} \left(\frac{\int_{\mathbb{R}^2} \mathbf{x} \left| \tilde{I}_{0,0}^m(\mathbf{x}) \right| d\mathbf{x}}{\int_{\mathbb{R}^2} \left| \tilde{I}_{0,0}^m(\mathbf{x}) \right| d\mathbf{x}} - \frac{\int_{\mathbb{R}^2} \mathbf{x} \left| \tilde{I}_{p,q}^m(\mathbf{x}) \right| d\mathbf{x}}{\int_{\mathbb{R}^2} \left| \tilde{I}_{p,q}^m(\mathbf{x}) \right| d\mathbf{x}} \right) , \quad (4.15)$$

where $|\Delta_{j,k}|$ denotes the number of elements in the set $\Delta_{j,k}$.

Proof. Let $j, k \in \mathbb{Z}$ be arbitrary but fixed and let $p, q \in \Delta_{j,k}$. Due to (4.11) there holds

$$\left| \tilde{I}_{p,q}^m(\mathbf{x} - ((\mathbf{s}_{j,k} - \mathbf{s}_{0,0}) + (\mathbf{t}_{p,q} - \mathbf{t}_{0,0}))) \right| \approx \left| \tilde{I}_{0,0}^m(\mathbf{x}) \right| .$$

Computing the center of mass on both sides we obtain

$$\frac{\int_{\mathbb{R}^2} \mathbf{x} \left| \tilde{I}_{p,q}^m(\mathbf{x} - ((\mathbf{s}_{j,k} - \mathbf{s}_{0,0}) + (\mathbf{t}_{p,q} - \mathbf{t}_{0,0}))) \right| d\mathbf{x}}{\int_{\mathbb{R}^2} \left| \tilde{I}_{p,q}^m(\mathbf{x} - ((\mathbf{s}_{j,k} - \mathbf{s}_{0,0}) + (\mathbf{t}_{p,q} - \mathbf{t}_{0,0}))) \right| d\mathbf{x}} \approx \frac{\int_{\mathbb{R}^2} \mathbf{x} \left| \tilde{I}_{0,0}^m(\mathbf{x}) \right| d\mathbf{x}}{\int_{\mathbb{R}^2} \left| \tilde{I}_{0,0}^m(\mathbf{x}) \right| d\mathbf{x}} . \quad (4.16)$$

Next, note that by a simple change of variables in the integral we obtain

$$\begin{aligned} & \int_{\mathbb{R}^2} \mathbf{x} \left| \tilde{I}_{p,q}^m(\mathbf{x} - ((\mathbf{s}_{j,k} - \mathbf{s}_{0,0}) + (\mathbf{t}_{p,q} - \mathbf{t}_{0,0}))) \right| d\mathbf{x} \\ &= \int_{\mathbb{R}^2} \mathbf{x} \left| \tilde{I}_{p,q}^m(\mathbf{x}) \right| d\mathbf{x} + ((\mathbf{s}_{j,k} - \mathbf{s}_{0,0}) + (\mathbf{t}_{p,q} - \mathbf{t}_{0,0})) \int_{\mathbb{R}^2} \left| \tilde{I}_{p,q}^m(\mathbf{x}) \right| d\mathbf{x}. \end{aligned}$$

Together with the fact that

$$\int_{\mathbb{R}^2} \left| \tilde{I}_{p,q}^m(\mathbf{x} - ((\mathbf{s}_{j,k} - \mathbf{s}_{0,0}) + (\mathbf{t}_{p,q} - \mathbf{t}_{0,0}))) \right| d\mathbf{x} = \int_{\mathbb{R}^2} \left| \tilde{I}_{p,q}^m(\mathbf{x}) \right| d\mathbf{x},$$

we obtain that (4.16) is equivalent to

$$\frac{\int_{\mathbb{R}^2} \mathbf{x} \left| \tilde{I}_{p,q}^m(\mathbf{x}) \right| d\mathbf{x} + ((\mathbf{s}_{j,k} - \mathbf{s}_{0,0}) + (\mathbf{t}_{p,q} - \mathbf{t}_{0,0})) \int_{\mathbb{R}^2} \left| \tilde{I}_{p,q}^m(\mathbf{x}) \right| d\mathbf{x}}{\int_{\mathbb{R}^2} \left| \tilde{I}_{p,q}^m(\mathbf{x}) \right| d\mathbf{x}} \approx \frac{\int_{\mathbb{R}^2} \mathbf{x} \left| \tilde{I}_{0,0}^m(\mathbf{x}) \right| d\mathbf{x}}{\int_{\mathbb{R}^2} \left| \tilde{I}_{0,0}^m(\mathbf{x}) \right| d\mathbf{x}}.$$

which after a reordering of the terms yields

$$((\mathbf{s}_{j,k} - \mathbf{s}_{0,0}) + (\mathbf{t}_{p,q} - \mathbf{t}_{0,0})) \approx \frac{\int_{\mathbb{R}^2} \mathbf{x} \left| \tilde{I}_{0,0}^m(\mathbf{x}) \right| d\mathbf{x}}{\int_{\mathbb{R}^2} \left| \tilde{I}_{0,0}^m(\mathbf{x}) \right| d\mathbf{x}} - \frac{\int_{\mathbb{R}^2} \mathbf{x} \left| \tilde{I}_{p,q}^m(\mathbf{x}) \right| d\mathbf{x}}{\int_{\mathbb{R}^2} \left| \tilde{I}_{p,q}^m(\mathbf{x}) \right| d\mathbf{x}}.$$

Summing over all indices $p, q \in \Delta_{j,k}$ and noting that $\mathbf{s}_{j,k}$ is independent of p, q we obtain

$$|\Delta_{j,k}| (\mathbf{s}_{j,k} - \mathbf{s}_{0,0}) + \sum_{p,q \in \Delta_{j,k}} (\mathbf{t}_{p,q} - \mathbf{t}_{0,0}) \approx \sum_{p,q \in \Delta_{j,k}} \left(\frac{\int_{\mathbb{R}^2} \mathbf{x} \left| \tilde{I}_{0,0}^m(\mathbf{x}) \right| d\mathbf{x}}{\int_{\mathbb{R}^2} \left| \tilde{I}_{0,0}^m(\mathbf{x}) \right| d\mathbf{x}} - \frac{\int_{\mathbb{R}^2} \mathbf{x} \left| \tilde{I}_{p,q}^m(\mathbf{x}) \right| d\mathbf{x}}{\int_{\mathbb{R}^2} \left| \tilde{I}_{p,q}^m(\mathbf{x}) \right| d\mathbf{x}} \right),$$

which together with (4.10) now yields the assertion. \square

The above proposition implies that under Assumption 4.1 the relative slopes $(\mathbf{s}_{j,k} - \mathbf{s}_{0,0})$ of the wavefront aberration ϕ on the subdomains $\Omega_{j,k}$ can be computed according to (4.15) by averaging the difference between the centers of mass of the subimages $\tilde{I}_{p,q}^m$ and $\tilde{I}_{0,0}^m$ over all indices $p, q \in \Delta_{j,k}$. This averaging is reminiscent of the averaging used in hardware based AO-OCT approaches described in Section 4.1. Furthermore, note the similarity of (4.15) in comparison to (3.15) for the subaperture correlation method.

5 Numerical Examples

In this section, we demonstrate the behaviour of our novel DAC method summarized in Algorithm 2 on numerical examples based on both simulated and experimental data.

5.1 Implementation

In order to implement our DAC method on a computer, a proper discretization needs to be chosen. Since OCT images are in practice given as complex-valued images on an $M \times N$ pixel grid, a natural choice for discretizing the image functions I and I^m is to consider them as piecewise constant functions on that same pixel grid. The continuous Fourier transforms can then be approximated by discrete Fourier transforms (DFTs).

The subdomains $\Omega_{j,k}$ and $\tilde{\Omega}_{p,q}$ used to define the subimages $I_{j,k}^m$ and $\tilde{I}_{p,q}^m$ via cut-outs in the Fourier plane are then simply rectangles with a size of $J \times K$ and $P \times Q$ pixels, respectively. Since the DFT of an $M \times N$ pixel image again has the dimension $M \times N$, only a finite number of subdomains $\Omega_{j,k}$ and $\tilde{\Omega}_{p,q}$ need to be considered. Furthermore, note that we want to have exact subdivisions of our $M \times N$ pixel grid into subdomains $\Omega_{j,k}$ as well as of the subdomains $\Omega_{j,k}$ into the subdomains $\tilde{\Omega}_{p,q}$. This is only possible if M, N are multiples of J, K , and J, K are multiple of P, Q , respectively. Hence, for a given OCT image one either has to choose J, K and P, Q appropriately, or change the size of the image itself, e.g. by cropping or by extending it with zeros.

The subimages $I_{j,k}^m$ and $\tilde{I}_{p,q}^m$ can then be defined as in (3.8) and (4.5), respectively; see also Figure 3.3. Note that in our implementation we consider the coordinate center to be located in the middle of the $M \times N$ pixel grid. Furthermore, instead of taking the cut-outs of the Fourier coefficients D^m , shifting them to the center of the $M \times N$ pixel grid and applying the inverse DFT, one can also embed them into a smaller $\tilde{M} \times \tilde{N}$ pixel grid before computing the inverse DFT. While this can improve the overall speed of the algorithm, it can have a negative effect on the reconstruction accuracy; see below.

In the second step of Algorithm 2, the (relative) shift vectors $\mathbf{v}_{j,k,p,q} = (\mathbf{s}_{j,k} - \mathbf{s}_{0,0}) + (\mathbf{t}_{p,q} - \mathbf{t}_{0,0})$ need to be estimated by matching the subimages $\tilde{I}_{p,q}^m$ and $\tilde{I}_{0,0}^m$. Since in our implementation these images only have a finite size and were computed using DFTs, these shifts have to be understood as circular shifts and thus limit the largest accurately detectable relative wavefront slope $(\mathbf{s}_{j,k} - \mathbf{s}_{0,0})$ to \pm half the pixel size of the subapertures $\Omega_{j,k}$ in each component direction. Furthermore, in order for the method to be sufficiently accurate, the estimation of these shifts has to be performed within a subpixel accuracy. Hence, in our implementation we have used a subpixel shift detection method called the *single-step DFT algorithm* proposed in [12], which also allows to manually set the desired subpixel accuracy. Note that the shift detection accuracy can also be improved by choosing larger values of \tilde{M} and \tilde{N} . However, this strongly increases the required computational costs and overall runtime of our algorithm. In contrast, by only working with local refinements the single-step DFT algorithm can achieve a much higher subpixel accuracy at a lower computational cost.

In the fourth step of Algorithm 2, the wavefront aberration ϕ has to be reconstructed from the relative slopes $(\mathbf{s}_{j,k} - \mathbf{s}_{0,0})$, for which a number of different algorithms are available. In our implementation, we use the CuReD method introduced in Section 2.2. Note that in general the wavefront reconstruction problem admits a unique solution only up to an additive constant. The CuReD algorithm selects a constant such that the resulting reconstruction has a zero mean. However, note that due to (3.5) the choice of the additive constant has no influence on the absolute value of the corrected image.

5.2 Simulated Data

In this section, we apply our novel DAC method summarized in Algorithm 2 to numerical examples based on simulated data. The initial point-source-like aberration-free image I is defined on an 350×350 pixel grid as follows: The DFT of the image is chosen such that it has a zero (spectral) phase, i.e., $\varphi(\xi) \equiv 0$, and an amplitude corresponding to the Fourier amplitude of the classic cameraman test image. Then, different wavefront aberrations ϕ are added according to the imaging model (3.4). Note that for an easier comparison, all wavefront aberrations were normalized to have a zero mean.

For reconstructing the wavefront, the 350×350 pixel grid was subdivided into 14^2 subdomains $\Omega_{j,k}$ each with a uniform size of 25×25 pixel. In turn, each of the subdomains $\Omega_{j,k}$ was subdivided into 5^2 subdomains $\tilde{\Omega}_{p,q}$ with a uniform size of 5×5 pixels. Hence, in total there are 196 subdomains $\Omega_{j,k}$ and 4900 subdomains $\tilde{\Omega}_{p,q}$.

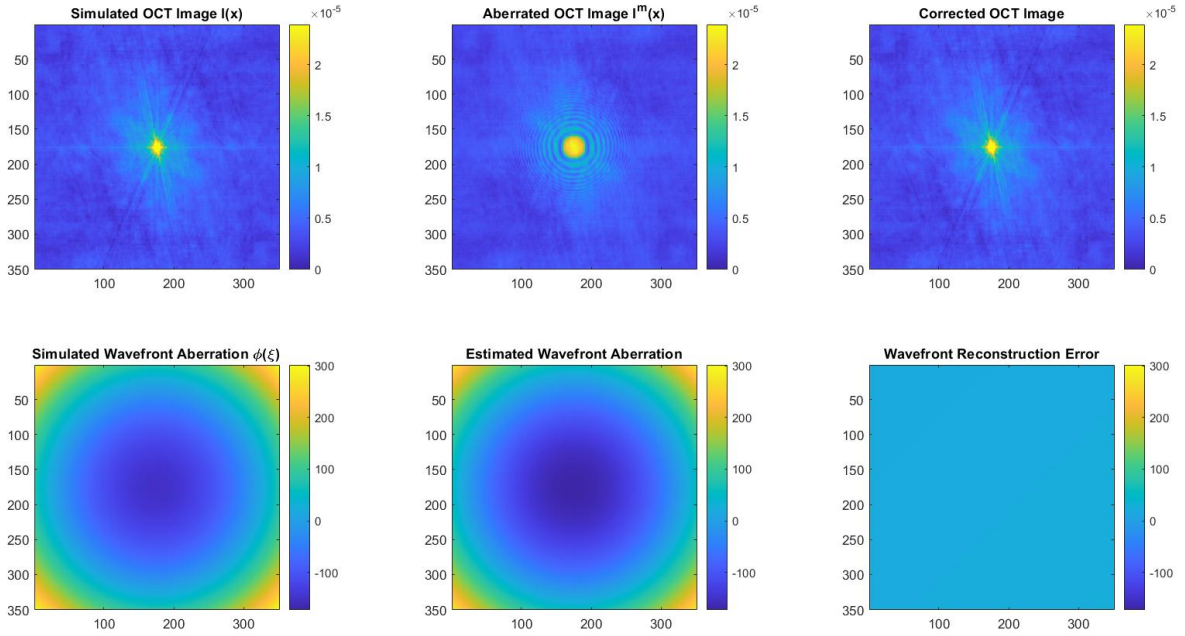


Figure 5.1: Simulation 1: OCT image with zero spectral phase and centered defocus wavefront aberration. Simulated, aberrated and corrected OCT image (top). Simulated and estimated wavefront aberration, and the reconstruction error, in radians (bottom).

Figure 5.1 depicts the results of the first test, where the simulated wavefront aberration ϕ corresponds to a centered defocus. We find that the reconstructed wavefront aberration closely matches the simulated one, with a relative error of only 1.1%. Consequently, also the corrected image closely resembles the aberration-free one.

Figure 5.2 depicts the results of the second test, which uses the same setup as before, but now with a more complex wavefront aberration ϕ . Again the reconstructed wavefront is closely resembling the simulated one, with a relative error of 6.73%. Note that since subaperture-based DAC methods reconstruct the wavefront aberration from computed slopes on the subdomains $\Omega_{j,k}$, the total number and size of those subdomains

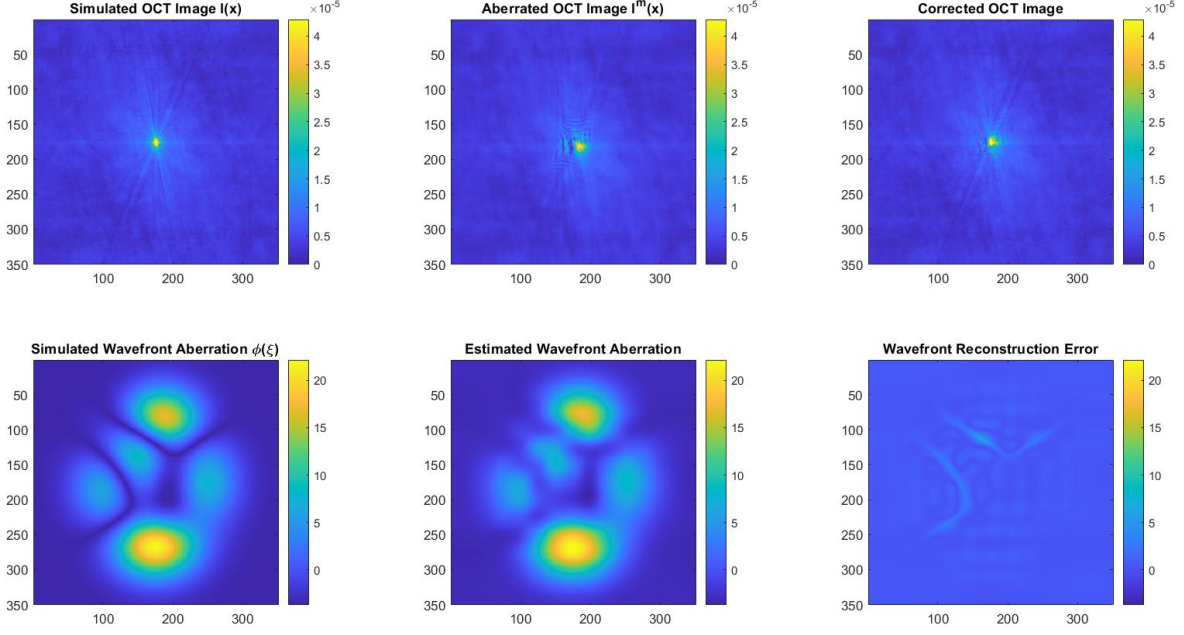


Figure 5.2: Simulation 2: OCT image with zero spectral phase and complex wavefront aberration. Simulated, aberrated and corrected OCT image (top). Simulated and estimated wavefront aberration, and the reconstruction error, in radians (bottom).

directly influences the amount of details of the aberrations which can be recovered. This explains the reconstruction error in the center-NW section of the wavefront aberration, in which its spatial variation is higher than in the remainder of the image. Note that in general a good balance has to be found when selecting the number/size of the subdomains $\Omega_{j,k}$ and $\tilde{\Omega}_{p,q}$. On the one hand, a large number of subdomains $\Omega_{j,k}$ leads to a large number of slopes $\mathbf{s}_{j,k}$ from which the wavefront aberration can eventually be reconstructed. On the other hand, if the size of the subdomains $\Omega_{j,k}$ is too small, only few subdomains $\tilde{\Omega}_{p,q}$ can be selected, and thus the statistical assumption (4.10) underlying the averaging process in our new DAC approach may no longer be valid. This effect is particularly relevant for the experimental OCT data considered below. Ultimately, this reflects the physical observation made in Section 4.1 that typically the wavefront aberration lives on a lower frequency than the spectral phase, in that the boundary between high and low frequency needs to be reflected in the size/number of subdomains $\Omega_{j,k}$ and $\tilde{\Omega}_{p,q}$. In other words, wavefront aberrations of a too large spatial variation can not be distinguished from the spectral phase of the object, and thus also not reconstructed or corrected for. Finally, note that with an increased number of subdomains the overall computational cost increases, which can pose a practical limitation.

For the next two experiments, we use the same wavefront aberrations as considered before, but now with a different aberration-free image I . In particular, we choose I such that it has the same spectral amplitude $|\mathcal{F}(I)(\xi)|$ as before, but now add a normally distributed spectral phase φ with a zero mean and a standard deviation of 0.5.

Figure 5.3 and Figure 5.4 depict the results of the third and fourth experiments,

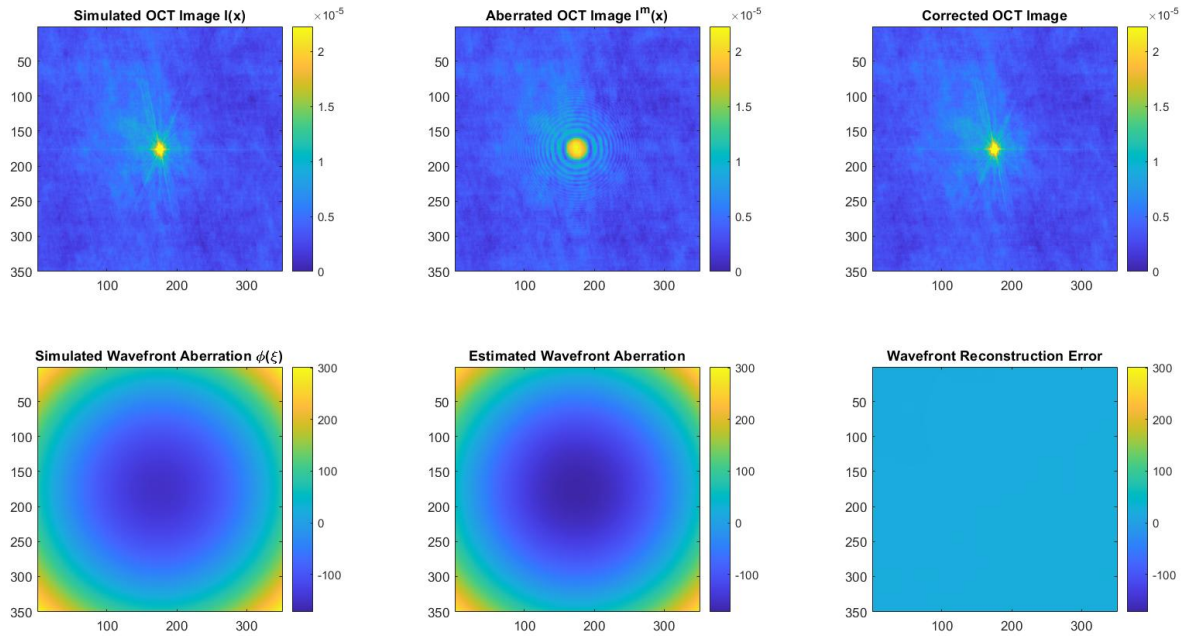


Figure 5.3: Simulation 3: OCT image with random spectral phase and centered defocus wavefront aberration. Simulated, aberrated and corrected OCT image (top). Simulated and estimated wavefront aberration, and the reconstruction error, in radians (bottom).

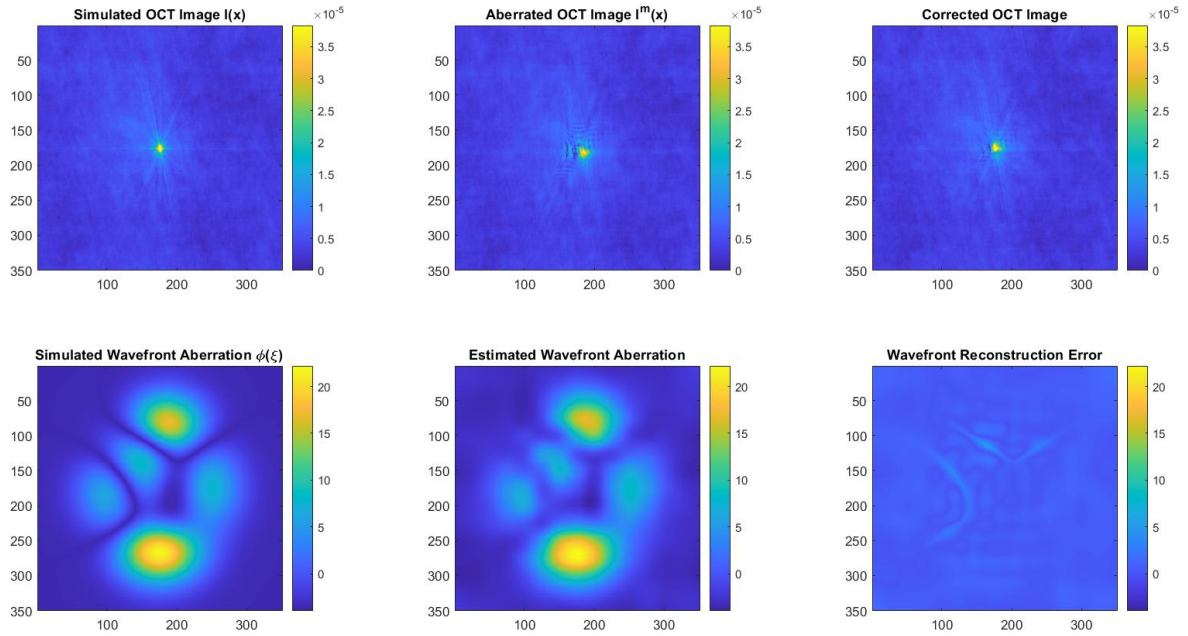


Figure 5.4: Simulation 4: OCT image with random spectral phase and complex wavefront aberration. Simulated, aberrated and corrected OCT image (top). Simulated and estimated wavefront aberration, and the reconstruction error, in radians (bottom).

which use this new aberration-free image I together with wavefront aberrations ϕ from the first and second experiment, respectively. As expected, due to the added random spectral phase φ , the reconstructed wavefronts are now less accurate than before, due to the slopes $\mathbf{t}_{p,q}$ averaged out by our method being only approximately constant on the subdomains $\Omega_{p,q}$. However, the reconstructed wavefronts still reasonably match the simulated ones, with the relative errors now being 1.1% and 7.1%, respectively.

5.3 Experimental Data

In this section, we apply our novel DAC method summarized in Algorithm 2 to measurement data from an actual OCT experiment. In particular, the image I^m is a manually defocused OCT image of multiple microbeads on a glass surface, recorded with the OCT system described in [17].

The experimental OCT image is given on a 350×350 pixel grid, which for the wavefront reconstruction was subdivided into 7^2 subdomains $\Omega_{j,k}$ with a uniform size of 50×50 pixel. In turn, each of those subdomains $\Omega_{j,k}$ was subdivided into 2^2 subdomains $\tilde{\Omega}_{p,q}$ with a uniform size of 25×25 pixel. Hence, in total there are 14 subdomains $\Omega_{j,k}$ and 56 subdomains $\tilde{\Omega}_{p,q}$. Figure 5.5 depicts the results of applying our novel DAC method to the experimental OCT data. Note first that the spectral phase $\arg(\mathcal{F}(I^m))$ depicted in the bottom right figure is mainly dominated by the spectral phase φ of the object, and that the experimentally applied defocus ϕ is not directly visible. Nevertheless, the defocus does have a sufficiently strong effect on the subimages $\tilde{I}_{p,q}^m$ such that our algorithm manages to reconstruct it accurately from their relative shifts. As a result, in comparison to the measured OCT image I^m , the microbead structure is clearly resolved in the digitally corrected OCT image. Note that the striped structure near the top center of the spectral phase $\arg(\mathcal{F}(I^m))$ slightly affects the reconstructed aberration in that area. If our algorithm were applied with a much larger number of subapertures, this and the similarly striped area in the middle right area of the spectral phase start to dominate the shift of the corresponding subimages $\tilde{I}_{p,q}^m$, ultimately degrading the reconstruction quality. This is also related to the fact that for a too large number of subdivisions the assumptions underlying our algorithm may no longer be valid. However, as the presented experimental results show, with a reasonable choice of subdivisions good aberration correction can be obtained completely digitally also on experimental data.

6 Conclusion

In this paper, we considered subaperture-based DAC approaches for the hardware-free wavefront aberration correction of OCT images. In particular, we introduced a mathematical framework for describing this class of approaches, which also resulted in a new understanding of the subaperture-correlation method introduced previously. Furthermore, based on the insight gained by this mathematical description, we developed a novel DAC approach requiring only minimal statistical assumptions on the spectral

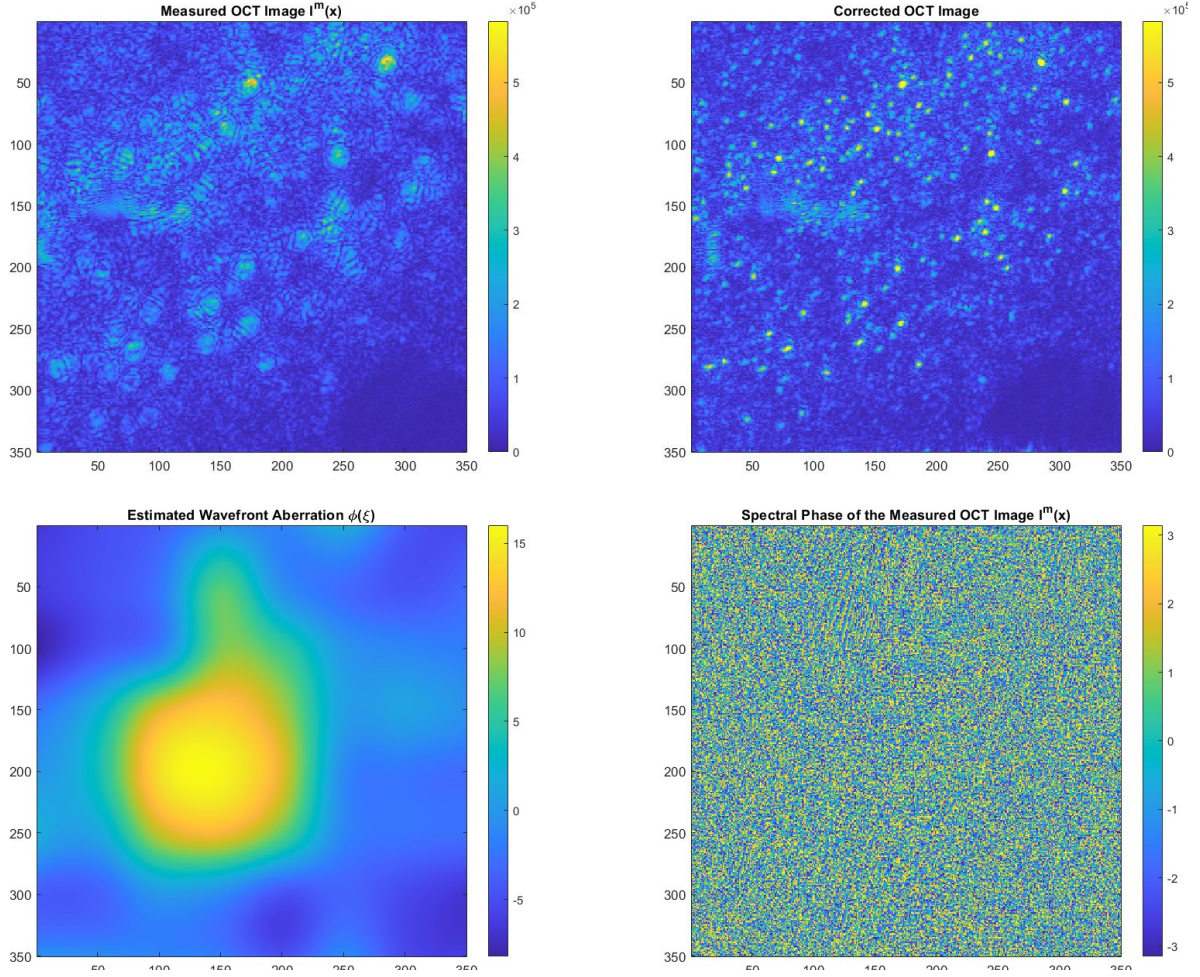


Figure 5.5: Results of our novel DAC approach applied to experimental OCT data. Top: measured and corrected en-face OCT image of microbeads. Bottom: estimated wavefront aberration in radians and spectral phase $\arg(\mathcal{F}(I^m))$ of the measured image (bottom).

phase of the scanned object. Finally, we demonstrated the applicability of our novel DAC approach via numerical examples based on both simulated and experimental data.

7 Support

The authors were funded by the Austrian Science Fund (FWF): project F6803-N36 (RL, MP), F6805-N36 (SH, RR), and F6807-N36 (ES), within the SFB F 68 “Tomography Across the Scales”.

References

- [1] S.G. Adie, B. W. Graf, A. Ahmad, P. S. Carney, and S. A. Boppart. Computational adaptive optics for broadband optical interferometric tomography of biological tissue. *Proceedings of the National Academy of Sciences of the United States of America*, 109(19):7175–80, 2012.
- [2] E. Brunner, J. Shatokhina, M. F. Shirazi, W. Drexler, R. Leitgeb, A. Pollreisz, C. K. Hitzenberger, R. Ramlau, and M. Pircher. Retinal adaptive optics imaging with a pyramid wavefront sensor. *Biomed. Opt. Express*, 12(10):5969–5990, 2021.
- [3] C. L. Chen and R. K. Wang. Optical coherence tomography based angiography [Invited]. *Biomed. Opt. Express*, 8(2):1056–1082, 2017.
- [4] M. A. Choma, M. V. Sarunic, C. H. Yang, and J. A. Izatt. Sensitivity advantage of swept source and Fourier domain optical coherence tomography. *Optics Express*, 11(18):2183–2189, 2003.
- [5] Johannes F. de Boer, Christoph K. Hitzenberger, and Yoshiaki Yasuno. Polarization sensitive optical coherence tomography - a review [Invited]. *Biomed. Opt. Express*, 8(3):1838–1873, 2017.
- [6] W. Drexler and J. G. Fujimoto, editors. *Optical Coherence Tomography - Technology and Applications*. Springer International Publishing, Switzerland, 2015. 2nd edition.
- [7] P. Elbau, L. Mindrinos, and L. Veselka. Development of mathematical models for quantitative OCT: A review. *AIMS Mathematics*, 8(2):2508–2531, 2023.
- [8] B. L. Ellerbroeck and C. R. Vogel. Inverse problems in astronomical optics. *Inverse Problems*, 25(6):063001 (37pp), 2009.
- [9] L. Gilles and B. Ellerbroeck. Shack-hartmann wavefront sensing with elongated sodium laser beacons: centroiding versus matched filtering. *Applied Optics*, 45(25):6568—6576, 2006.
- [10] P. Godara, A. M. Dubis, A. Roorda, J. L. Duncan, and J. Carroll. Adaptive optics retinal imaging: Emerging clinical applications. *Optometry and Vision Science*, 87(12):930–41, 2010.
- [11] J. W. Goodman. *Introduction to Fourier Optics*. McGraw-Hill physical and quantum electronics series. W. H. Freeman, 2005.
- [12] M. Guizar-Sicairos, S. T. Thurman, and J. R. Fienup. Efficient subpixel image registration algorithms. *Opt. Lett.*, 33:156–158, 2008.
- [13] D. Hillmann, H. Spahr, C. Hain, H. Sudkamp, G. Franke, C. Pfäffle, C. Winter, and G. Hüttmann. Aberration-free volumetric high-speed imaging of in vivo retina. *Scientific Reports*, 6(1):35209, 2016.
- [14] H. Hofer, P. Artal, B. Singer, J. L. Aragón, and D. R. Williams. Dynamics of the eye’s wave aberration. *J. Opt. Soc. Am. A*, 18(3):497–506, 2001.
- [15] L. Krainz, E. Sherina, S. Hubmer, M. Liu, W. Drexler, and O. Scherzer. Quantitative Optical Coherence Elastography: A novel Intensity-based Inversion Method versus Strain-based Reconstructions. *IEEE Journal of Selected Topics in Quantum Electronics*, 29(4):1–16, 2022.
- [16] A. Kumar, W. Drexler, and R. A. Leitgeb. Subaperture correlation based digital adaptive optics for full field optical coherence tomography. *Opt. Express*, 21(9):10850–10866, 2013.
- [17] A. Kumar, S. Georgiev, and M. Salas R. A. Leitgeb. Digital adaptive optics based on digital lateral shearing of the computed pupil field for point scanning retinal swept source OCT. *Biomedical Optics Express*, 12(3):1577–92, 2021.
- [18] A. Kumar, T. Kamali, R. Platzer, A. Unterhuber, W. Drexler, and R. A. Leitgeb. Anisotropic aberration correction using region of interest based digital adaptive optics in Fourier domain OCT. *Biomedical Optics Express*, 6(4):1124–34, 2015.

- [19] A. Kumar, L. M. Wurstler, M. Salas, L. Ginner, W. Drexler, and R. A. Leitgeb. In-vivo digital wavefront sensing using swept source OCT. *Biomed. Opt. Express*, 8(7):3369–3382, 2017.
- [20] R. A. Leitgeb and B. Baumann. Multimodal Optical Medical Imaging Concepts Based on Optical Coherence Tomography. *Frontiers in Physics*, 6, 2018.
- [21] R. A. Leitgeb, F. Placzek, E. A. Rank, L. Krainz, R. Haindl, Q. Li, M. Liu, A. Unterhuber, Schmoll T, and W. Drexler. Enhanced medical diagnosis for dOCTors: a perspective of optical coherence tomography. *Journal of Biomedical Optics*, 26(10):100601, 2021.
- [22] F. Lexer, C. K. Hitzenberger, A. F. Fercher, , and M. Kulhavy. Wavelength-tuning interferometry of intraocular distances. *Applied Optics*, 36(25):6548–6553, 1997.
- [23] Y. Z. Liu, F. A. South FA, Y. Xu, P. Scott Carney, and S. A. Boppart. Computational optical coherence tomography. *Biomed Opt Express*, 8(3):1549–74, 2017.
- [24] M. Pircher, C. K. Hitzenberger, and U. Schmidt-Erfurth. Polarization sensitive optical coherence tomography in the human eye. *Prog Retin Eye Res*, 30(6):431–451, 2011.
- [25] M. Pircher and R. J. Zawadzki. Review of adaptive optics OCT (AO-OCT): Principles and applications for retinal imaging. *Biomed Opt Express*, 8(5):2536–62, 2017.
- [26] B. C. Platt and R. Shack. History and principles of shack-hartmann wavefront sensing. *Journal of Refractive Surgery*, 17(5):S573–S577, 2001.
- [27] J. Primot. Theoretical description of shack–hartmann wave-front sensor. *Optics Communications*, 221(1):81–92, 2003.
- [28] R. Ragazzoni. Pupil plane wavefront sensing with an oscillating prism. *Journal of Modern Optics*, 43(2):289–293, 1996.
- [29] F. Roddier. *Adaptive optics in astronomy*. Cambridge University Press, 1999.
- [30] M. Rosenstainer. Cumulative Reconstructor: fast wavefront reconstruction algorithm for Extremely Large Telescopes. *J. Opt. Soc. Am. A*, 28(10):2132–2138, 2011.
- [31] M. Rosenstainer. Wavefront reconstruction for Extremely Large Telescopes via CuRe with Domain Decomposition. Technical Report E-TRE-AAO-528-0018, Austrian In-Kind Contribution - AO, 2011.
- [32] J. M. Schmitt. OCT elastography: imaging microscopic deformation and strain of tissue. *Optics Express*, 3(6):199–211, 1998.
- [33] N. D. Shemonski, F. A. South, Y.-Z. Liu, S. G. Adie, P. Scott Carney, and S. A. Boppart. Computational high-resolution optical imaging of the living human retina. *Nat Photon*, 9(7):440–3, 2015.
- [34] M. F. Shirazi, J. Andilla, N. Lefaudeux, C. Valdes, F. Schwarzhans, M. Durand, K. Ntassis, D. A. De Jesus, L. S. Brea, K. Gocho, J. Gautier, C. Eckmann-Hansen, M. E. W. Torm, A. Amini, S. Klein, T. Van Walsum, K. Grieve, M. Paques, M. Larsen, P. Loza-Alvarez, X. Lev-ecq, N. Chateau, and M. Pircher. Multi-modal and multi-scale clinical retinal imaging system with pupil and retinal tracking. *Sci Rep-Uk*, 12, 2022.
- [35] Vladimir Y. Zaitsev, Alexander L. Matveyev, Lev A. Matveev, Alexander A. Sovetsky, Matt S. Hepburn, Alireza Mowla, and Brendan F. Kennedy. Strain and elasticity imaging in compression optical coherence elastography: The two-decade perspective and recent advances. *Journal of Biophotonics*, 14(2):e202000257, 2021.
- [36] M. Zhariy, A. Neubauer, M. Rosenstainer, and R. Ramlau. Cumulative wavefront reconstructor for the Shack-Hartmann sensor. *Inverse Problems and Imaging*, 5:893–913, 2011.